STRUCTURE OF EVENTS WITH A PARTICLE AT LARGE TRANSVERSE MOMENTUM IN PROTON – PROTON COLLISIONS AT THE CERN ISR

Inaugural-Dissertation zur Erlangung der
Doktorwürde der Mathematisch-Naturwissenschaftlichen
Gesamtfakultät der

RUPRECHT-KARLS-UNIVERSITÄT HEIDELBERG

vorgelegt von

Diplom-Physiker Werner F. Herr
aus Schottenstein

– 1985 –

Gutachter: Prof. Dr. Eike-Erik Kluge

Prof. Dr. Otto Nachtmann

ABSTRACT

The structure of events with a particle with large transverse momentum has been studied for proton-proton collisions at a centre-of-mass energy of $\sqrt{s}$ = 62.2 GeV. The experiment was performed with the Split-Field-Magnet detector at the CERN Intersecting Storage Rings and events were recorded with high-p_T particles with $p_T > 2$ GeV/c produced at polar angles around 45° and 20°.

The distributions of charged particles in the jet recoiling against the high-p_T particle have been measured as a function of the fragmentation variable $x_E = p_T/p_T^{tri}$.

The production of high-p_T particles is usually interpreted in the quark parton model as the hard collision of proton constituents. The asymmetry and charge composition of the recoil jet and their correlation with the flavour of the high-p_T particle supports this qualitative picture. Model calculations using first order Quantum Chromodynamics (QCD) and phenomenological fragmentation model cannot explain the particle distribution in the recoil jet.

* * * * * *

Die Struktur von Ereignissen mit einem Teilchen mit hohem Transversalimpuls wurde für Proton-Proton Wechselwirkungen bei einer Schwerpunktsenergie von $\sqrt{s}$ = 62.2 GeV untersucht. Das Experiment wurde mit dem Split-Field-Magnet Detektor an den CERN Protonenspeicherringen durchgeführt und Ereignisse mit einem Teilchen mit $p_T > 2$ Gev/c bei Polarwinkeln von 45° und 20° wurden aufgezeichnet.

Die inklusiven Verteilungen der geladenen Teilchen im Jet gegenüber dem Teilchen mit hohem Transversalimpuls wurden als Funktion der Fragmentationsvariable $x_E = p_T/p_T^{tri}$ bestimmt.

Die Produktion von Teilchen mit hohem Transversalimpuls wird im Quark-Parton Modell als die harte Streuung zweier Konstituenten der wechselwirkenden Protonen beschrieben. Die Asymmetrie und die Ladungszusammensetzung der Teilchen in diesem Rückstossjet und deren Korrelationen mit der Natur des Triggerteilchens bestätigen qualitativ dieses Modell. Detaillierte Modellrechnungen im Rahmen der Quantenchromodynamik (QCD) mit phänomenologischen Fragmentationsmodellen konnen die Verteilung der Sekundärteilchen jedoch nicht zufriedenstellend beschreiben.

CONTENTS

1. INTRODUCTION

In contrast to the well established theory of electromagnetic and weak interactions, no complete theory exists which could explain or derive the features of strong interactions between hadrons. A good candidate however is a gauge theory called Quantum Chromodynamics (QCD) (see e.g. FRI73,POL73) in which the interaction between hadrons is mediated by the exchange of gluons. Since reliable QCD calculations are based on perturbative techniques, only reactions with a large momentum transfer, Q^2, can be used to test the theory because the strong coupling constant $\alpha_s(Q^2)$ is small only for large values of Q^2. Interactions with a large momentum transfer are deep inelastic lepton-nucleon scattering or large angle hadron-hadron scattering where particles with large transverse momenta are produced. The study of hard hadron-hadron interactions allows therefore to get direct access to fundamental strong interactions between the hadron constituents, namely quark-quark, quark-gluon, and, due to the non-Abelian structure of QCD, gluon-gluon interactions. The direct interaction of gluons can only be observed in hadron-hadron interaction while in deep inelastic lepton-nucleon scattering or electron-positron scattering the gluonic interaction is indirectly "observed" through the amount of scale breaking effects. Hard hadronic collisions appear as the result of a hard elastic scattering process between the hadron constituents and their subsequent fragmentation into observable particles, forming "jets" of hadrons with substantially higher transverse momenta than for those from normal inelastic hadron-hadron collisions. For such deep-inelastic hadron-hadron collisions, two transverse jets at approximately opposite azimuth originate from the scattered partons (mainly quarks or gluons), and two longitudinal jets are fragments of the hadron remnants which are not involved in the scattering process. This expected four jet structure was established by different types of experiments. It was first confirmed by experiments triggering on a particle with large transverse momentum (see e.g. DEL77) and later verified by experiments selecting events with a large transverse energy (see e.g. ARN83a,BAG83). The diverse types of scattering processes should manifest in different quantum number structures of the jets. It will be shown that the selection of events with a single identified particle with large transverse momentum is a powerful tool to study the nature of the underlying parton scattering processes. Therefore it is necessary to study the structure of the complete event and requires an accelerator with a high interaction rate to be sensitive to the small cross section for hard collisions. The CERN Intersecting Storage Rings (ISR) providing proton-proton collisions at high centre-of-mass energies and high luminosities are a perfect environment for those studies. We have recently published measurements on the structure of secondaries accompanying the large transverse momentum particle (BRE84c, BRE84g) appearing as fragments in the "trigger-jet". In the present analysis the structure of the second transverse jet, the "away-jet", will be investigated. After a brief description of the Quark-Parton model (QPM) and different fragmentation schemes the densities of negative and positive particles are determined as a function of the fragmentation variable $x_E = p_T/p_T^{tri}$. The spatial configuration of the two transverse jets contains information about the kinematics of the scattering process and can therefore be used to enrich specific subprocesses because the dynamics of the proton constituents is different for the various types. The observed charge structure of the secondaries in the away-jet allows one to draw conclusions about the charge of the scattered partons and therefore makes it possible to distinguish between different parton-parton subprocesses.

It will be shown that these measurements are strongly correlated with the nature of the large transverse momentum particle and are dependent on the scattering angle. These correlations can be qualitatively understood within the quark-parton model, irrespective of specific fragmentation models.

The results will be compared to detailed model calculations based on the Quark-Parton model and first order QCD.

2. EXPERIMENTAL SETUP

2.1 THE INTERSECTING STORAGE RINGS

The advantage of experiments with two colliding beams over those with a fixed target is the substantially higher energy available for the production of particles in beam-beam interactions. For experiments at conventional particle accelerators most of the energy is shared as kinetic energy between the particles moving in the laboratory system. With two colliding beams the centre-of-mass-system (CMS) is at rest in the laboratory system and no energy is wasted in the form of CMS-motion. The CERN Intersecting Storage Rings (ISR) consist of two concentric vacuum ring pipes filled with protons running in opposite directions. They cross each other in eight interaction regions, where proton proton interactions can be studied, with an angle of about 15°. A schematic view of the accelerator system together with the beam transport lines is shown in Fig.2.1. After ionization the protons are sent into a linear accelerator (LINAC) and pushed to a momentum of 50 MeV/c and subsequently accumulated and accelerated in a booster synchrotron. From this booster bunches with about 10^{13} protons each bunch are transferred to the CERN Proton Synchrotron (CPS) and accelerated to momenta between 11.8 GeV/c and 26.5 GeV/c. After injection into the ISR the protons are moved from their injection orbit to an orbit with a larger radius and eventually accelerated to the final momenta of up to 31.4 GeV/c. During this filling process the proton bunches are debunched to form a continous current over the ring. Several hundred bunches (each bunch with up to 150 mA) from the CERN Proton Synchrotron are stacked into each ring to reach the required currents of up to 40 A in each ring. All data analyzed in this study were taken with the highest possible ISR energy of 31.4 GeV per proton.

For a given reaction, the interaction rate is proportional to the reaction cross section:

$$dN_i/dt = L \cdot \sigma_i$$

The proportionality constant L is called luminosity. A maximum luminosity of $2.0 \cdot 10^{31}$ cm^2 s^{-1} was obtained at the ISR which implies an interaction rate of about 900 kHz.

A measurement of the luminosity is performed by the Van der Meer method (VDM68) and continously monitored with scintillation counters.

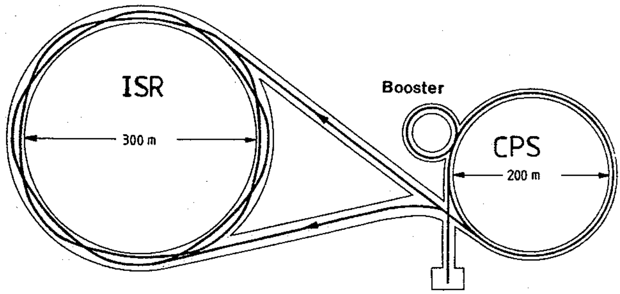

Fig.2.1: Schematic layout of the CERN Proton Synchrotron (CPS) and the ISR.

The high luminosity and therefore high event rate at the ISR allows the study of rare events with a small cross section like the production of heavy flavours, events with particles at large transverse momentum, and elastic events with large momentum transfer.

2.2 THE SPLIT-FIELD-MAGNET DETECTOR

The Split-Field-Magnet (SFM) detector is a general purpose detector situated at the interaction region 4 (I4) at the CERN Intersecting Storage Rings (BEL75, BOU74, BOU75). It is capable to detect and measure charge and momentum of charged particles in almost the full solid angle and allows particle identification in part of the phase space. The Split-Field-Magnet detector has been in successful operation at the ISR between 1974 and 1983 and has been upgraded and improved several times during this period (BEL78). The experimental setup which was used to record the data for this analysis will be described more thoroughly in the following chapters.

2.2.1 The Split-Field-Magnet

To allow the measurement of the charge and momentum of all particles, the spectrometer is embraced in a magnetic field. This magnetic field is provided by the Split-Field-Magnet (SFM). The layout of the Split-Field-Magnet is displayed in Fig.2.2 for two different views.

To minimize the distortions of the beams by the magnetic field of the spectrometer, the field directions (perpendicular to the incoming particles in the laboratory system) are of opposite directions in the two symmetric parts of the magnet. Remaining perturbations are removed by two compensator magnets in front and behind the interaction region. The main parameters of the magnet are given in table 2.1.

For different proton momenta different field levels are used. The collision angle α of the two beams varies with the beam momenta and with the magnetic field as given in table 2.2 (BRY73).

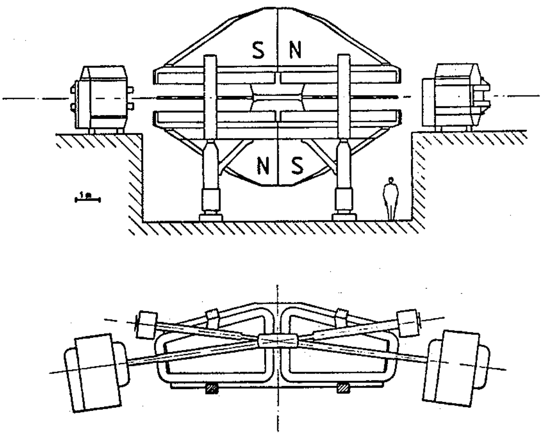

Fig.2.2: Split-Field-Magnet for two different views.

For the reconstruction of the particle's charge and momentum it is necessary to know the magnetic field at any given space point in the fiducial volume of the spectrometer. Therefore the field has been measured in one quadrant at 25000 locations using a Hall probe. To provide the magnetic field in quadrants other than the measured one, the symmetry of the Split-Field-Magnet was used. For the description of the field within the reconstruction program, 15 * 20 * 30 cm^3 in size) and parametrized in each of these boxes, by polynomials with a maximum order of three (MET74). The total number of coefficients necessary for the description of the field is about 80000.

Total length	10.3	m
Height	7.2	m
Width	2.0-3.0	m
Distance between pole pieces	1.1	m
Magnetic field volume	28.0	m^3
Total iron weight	840	t
Total copper weight	42	t
Maximum current	6250	A
Voltage rating	650	V
Power consumption	4	MW
Maximum field	1.14	T

Table 2.1: Split-Field-Magnet parameters

SFM field (T)	beam momentum (GeV/c)				
	31.460	26.588	22.505	15.376	11.780
1.00	17.477	17.971	18.552	---	---
0.85	17.080	17.503	17.998	19.494	---
0.65	16.532	16.854	17.232	18.372	19.471
0.50	16.113	16.359	16.647	17.516	18.353
0.00	14.773	14.773	14.773	14.773	14.773

Table 2.2: Beam crossing angles at the SFM.
Box indicates running conditions for the data used in this analysis.

2.2.2 The Spectrometer

The Split-Field-Magnet spectrometer consists of an arrangement of multiwire proportional chambers (MWPC) with approximately 70000 sensitive wires (BOU74, BEL75, BOU75). Multiwire proportional chambers fulfil many features necessary for a successful operation of a detector at an accelerator with a high event rate like the ISR:

- Capability to stand high event rates (up to 900 kHz) with a good time resolution and a low deadtime.
- High efficiency for the detection of several charged particles passing the same detector element independently. This implies a good spatial resolution roughly irrespective of the angle of incidence and the momentum of the particles.
- Small amount of material to keep the background from secondary interactions and conversions as small as possible and to avoid strong distortion of primary particle trajectories by multiple scattering and energy loss.
- The possibility to use the detector within the trigger system select rare events amidst the bulk of normal events. The reduction factors needed are in the order 10^5.

The principle layout of the spectrometer is sketched in Fig.2.3. The spectrometer is divided into the central detector (BOU74) surrounding the interaction region and two forward telescopes (BOU74) for the detection of particles produced at small polar angles close to the beam pipe. Near the interaction region two small chambers with analog readout measure the energy loss whilst all other chambers are read out to provide a yes/no decision as a position measurement.

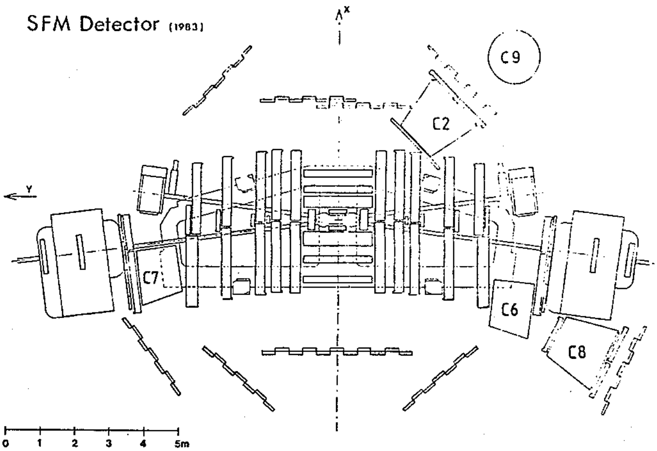

Fig.2.3: Top view of the Split-Field-Magnet detector.

In three regions of the detector the trigger system is sensitive to particles with a large transverse momentum. Particle identification in these regions is performed using the Cherenkov counters marked as C2,C6,C7,C8, and C9 in Fig.2.3. They cover the region for particles produced at polar angles around Θ = 10°, 20° and 45°.

Construction of the chambers

To avoid significant acceptance losses due to thick chamber frames the chambers are build as a frameless, self-supporting construction of a foam sandwich type (Fig.2.4). The polyurethane foam plane with a layer of about 10 µm silver constitutes the cathode plane and the mechanical chamber support which gives a large acceptance with minimum weight. The sensitive wires consist of gold-plated tungsten with 20 µm diameter. They are supported at their ends on 5 mm wide epoxy frames. Support lines every 50 cm compensate the displacement of the wires due to electrostatic forces. The distance between two wires is 4 mm or 2 mm and the gap between the cathode planes and the wires is 8 mm or 5 mm. A maximum number of 512 wires form one chamber plane. Up to 11 of those planes are stacked together to build one physical chamber.

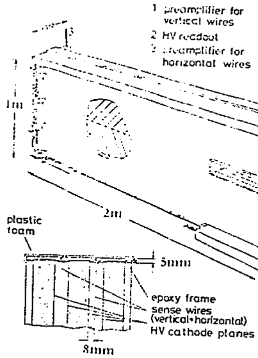

Fig.2.4: Layout of a multiwire proportional chamber at the SFM.

The planes succeed one another with different orientations of the wires to provide spatial information for the track: horizontal, vertical, and inclined wire planes in a certain order. Some smaller chambers in the forward telescopes do not have inclined wires. The chambers in the two forward telescopes are build around the beam pipe to avoid acceptance losses around the incoming and the outgoing beam directions.

All chambers are filled with a gas mixture, composed of 54% argon, 39% isobutane, and 7% methylal.

Electronic chain

The signals from the wires are preamplified in the experimental area and transmitted through twisted pair cables over a distance of 66 m to the counting room. After the signals are passed through a discriminator (D), shaped wire signals are input to the fast trigger logic (Fig.2.5). In the case the decision of the fast trigger logic is positive, a STROBE signal of 140 ns length is generated to open a gate and the signal is read into a memory unit (FF). The signals from the discriminators have to be delayed during the time required by the fast trigger logic to make sure that they arrive at the gate together with the STROBE signal. The stored signals from the memory units are used by the slow trigger logic to perform a more refined decision and the wire signals are read out onto a data bus for the data acquisition if the final trigger decision is positive.

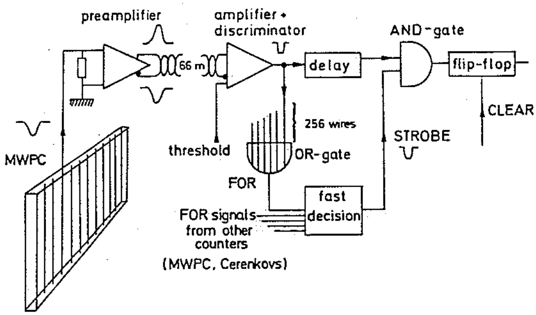

Fig.2.5: Electronic chain for a single wire.

Performance

1. Spatial resolution

For a particle passing perpendicular to a wire plane the theoretical value for the possible resolution is:

$$s = d/\sqrt{12}$$

where d is the distance between two sensitive wires.

For a particle with an angle of incidence different from 90° the resolution is also dependent on this angle α and varies between the extreme values:

$$\sigma^{max} = d/\sqrt{12} \qquad \text{for: } \tan(\alpha)=(n-1)\cdot d/2g \qquad (n=1,2,..)$$

and

$$\sigma^{min} = \sigma^{max}/2 \qquad \text{for: } \tan(\alpha)=(2n-1)\cdot d/4g \qquad (n=1,2,..)$$

where g is the distance between the wire and the cathode plane (FIS75).

For the wire distance of 4 mm used for this experiment, an average spatial resolution of 0.9 mm is theoretically possible. However, under running conditions the actual spatial resolution is a function of the chamber high voltage and the threshold of the discriminators since they are tuned to be most efficient for particle trajectories perpendicular to the wire planes.

2. Time resolution

The time resolution of a single wire is approximately 60 ns, but the real time resolution of the spectrometer is given by the length of the shaped signals which is 110 ns. During the time window defined by the STROBE signal (140 ns) the information from the wires can be read into the memory units. This window is longer than the shaped wire signals to make sure that signals from chambers at different distances from the interaction regions can be read in correctly. In the case that two events happen independently within the time window of the STROBE, it is possible that information from the second event is partly read out together with the triggering event. With a total interaction rate of $4 \cdot 10^5$ Hz this should occur in 7% of all events. This was verified experimentally using a random trigger (i.e. a clock) to start the data acquisition procedure. The vertices of such double events are generally well separated and it is possible to distinguish tracks from two different events.

2.3 THE LARGE P_T TRIGGER

The cross section for a hard scattering process yielding a particle with a transverse momentum larger than 4 GeV/c is in the order of 10^{-32} cm² compared to a total cross section for normal inelastic events of about $4.0 \cdot 10^{-27}$ cm². In order to be sensitive to such a small cross section and to suppress the large background from normal inelastic events, a trigger system is necessary which works efficiently for particles with large transverse momentum, has a large suppression factor for unwanted events, and a short dead time. At the Split-Field-Magnet detector the multiwire proportional chambers are used in a self-triggering mode to achieve this goal. A top view of the SFM detector is shown in Fig.2.3. The shaded areas indicate the acceptance of the three different triggers for particles with large transverse momentum at polar angles around Θ = 10°, 20° and 45°. The trigger logic uses three levels of decision. A sketch of the hierarchy of trigger levels is given in Fig.2.6.

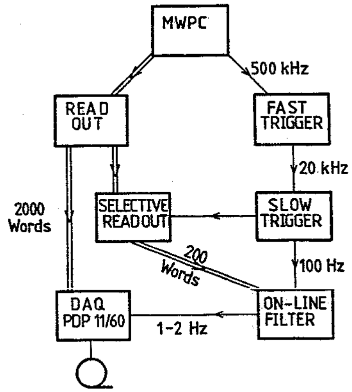

Fig.2.6: Trigger level hierarchy at the SFM detector with event rates and reduction factors.

The FAST trigger level

For the first (FAST) trigger level a fast or (FOR) signal is build by a group of 256 wires of one chamber plane. A FOR signal is generated if at least one wire in a given plane had a signal. The fast decision is a coincidence of FOR signals from chamber planes in the region of the trigger track (trigger telescope). The necessary time for this decision is approximately 500 ns and the suppression factor is in the order of 20-30. This factor depends on the trigger region and is different for large p_T particles at Θ^{tri} = 10°, 20°, and 45°.

The SLOW trigger level

With a signal from the fast trigger level (STROBE signal) the wire signal is read into memory units (flip flops) and available until a CLEAR signal arrives to erase the contents of the memory units. During the time of the slow decision the detector is insensitive to all arriving events. Therefore it is important to have a large suppression factor against unwanted events already at the FAST trigger level to avoid a large dead time of the detector. The signals from the flip flops are worked up into a memory or (MOR) of a group of 16 or 8 adjacent wires in one plane. A MOR signal is generated if at least one out of the wires in such a group is set. The MOR signals from successive planes are grouped into coincidence matrices to form "roads" which follow the wanted track trajectories. This roads are designed and optimized using generated tracks (PAN82). The decision time for the SLOW trigger level is about 2 µs with a reduction factor of 100-200.

On-line filtering

As a third trigger level (FILTER) a PDP 11/20 computer was used as an on-line filter (FRE81). A selected subset of the chamber coordinates inside the trigger region is read out and a track reconstruction is performed. The track momentum is estimated using the same algorithm as it is used later in the off-line track reconstruction (NOR78). The event is recorded whenever a track was successfully reconstructed and the calculated transverse momentum of the track candidate is above threshold. The time necessary for this decision is approximately 5 ms with a further reduction factor of 10-50 depending on the cut off in the transverse momentum and the trigger region.

2.4 THE TIME-OF-FLIGHT SYSTEM

One common method to determine the mass of a particle is the simultaneous measurement of its velocity and momentum. In this experiment the momentum of a particle is measured with multiwire proportional chambers and the velocity is determined by the measurement of the time of flight of the particle between two separated space points.

The Experimental layout

The Time-Of-Flight (TOF) system at the Split-Field-Magnet detector consists of 67 scintillation counters positioned in 8 clusters surrounding the magnetic spectrometer covering about 60.3 m² equivalent to 1.6 sr of the solid angle. The size of each scintillation counter is 225·2·40 cm³ and at either end a photomultiplier records the light from the scintillators. The distance of the scintillation counters from the interaction region varies between 3.5 m and 6.0 m. Another 14 smaller counters (100·2·40 cm³) are placed in the forward directions around the outgoing beams and serve at the same time as a luminosity-monitor. The electronic chain for one channel of the Time-of-Flight system is displayed in Fig.2.7.

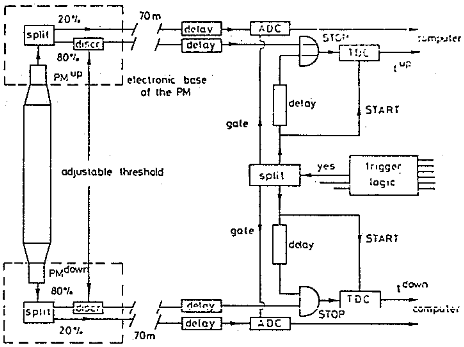

Fig.2.7: Electronic chain for one channel of the Time-Of-Flight system at the Split-Field-Magnet detector.

All signals from the photomultipliers are split into two parts, 20% and 80%, where the bigger one is read out into a TDC unit to get precise time information and the smaller one is read out by ADC units. A START signal from the trigger logic is used to start all TDC's independently and they are stopped either individually by a signal from the photomultiplier or by a common STOP signal which is derived from the delayed START signal. The time of the interaction t_0 is determined off-line and the procedure is described in section 3.1.3.

Calibration

The time delay of the signal due to the electronic chain is different for each scintillation counter. For the time of flight analysis this calibration constant has to be known and is determined experimentally.

A laser light source (N_2, spark gap, (HAN80)) was installed remote from the spectrometer and the light was distributed through equally long quartz light fibres to the centre of each scintillation counter and, in addition, directly into a separate photomultiplier which was used as a start counter for the TDC's and as an "event trigger". The "events" of this type are read out into ADC and TDC units and could be used either online or offline for the calibration and testing of the system.

Performance

It is possible to identify pions, kaons, and protons up to a momentum of 0.8 GeV/c and to distinguish protons from lighter particles up to a particle momentum of 2.0 GeV/c with a confidence level of 3 standard deviations. The time resolution of the full TOF system was determined to be of the order of 1.2 ns (FWHM). A typical mass distribution for tracks evaluated with the time of flight measurement at the Split-Field-Magnet detector is shown in Fig.2.8.

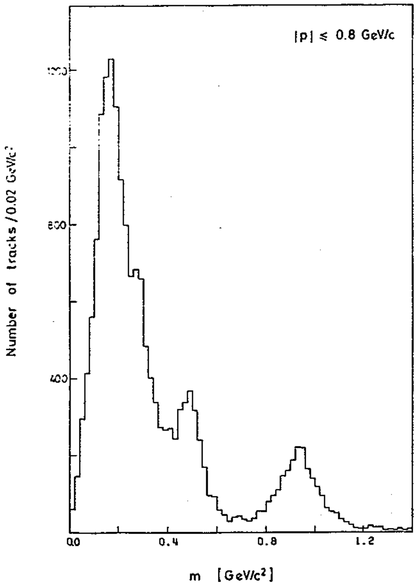

Fig.2.8: Mass distribution measured with the TOF system at the SFM detector.

2.4.1 Cherenkov counters

For the purpose of trigger particle identification, five Cherenkov counters (C2,C6,C7,C8 and C9 in Fig.2.3) were installed at the Split-Field-Magnet detector. Two counters, C2 and C9, cover the trigger telescope around $\Theta = 45°$, another two counters, C6 and C8, identify trigger particles at $\Theta = 20°$ and the counter C7 was put into the 10° trigger telescope.

Construction of the counters

All counters are gas filled threshold Cherenkov counters. Three different types were used in this experiment. The counters C2 and C8 are rectangular boxes (Fig.2.9) filled with Freon 114 (n = 1.00108) at atmospheric pressure and have thresholds of 3.0 GeV/c for pions and 10.6 GeV/c for kaons to produce light.

Four spherical mirrors collect the light produced in the active gas volume and focuse it onto light catchers with corresponding photomultipliers (KOR76). The photomultipliers are passively shielded against the influence of the magnetic field of the spectrometer by µ-metal and iron tubes while actively shielded with a compensation coil inside the µ-metal shield which produces an adjustable field to compensate for remaining distortions.

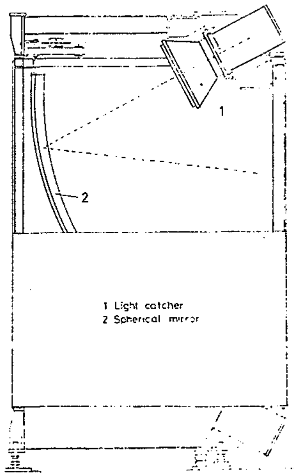

Fig.2.9: Layout of the Cherenkov counters C2 and C8.

The second type of Cherenkov counter (C6 and C7) is smaller and used to identify particles produced at small polar angles in the forward telescopes (HAN80). The layout of these counters is shown in Fig.2.10 for two different views.

The device consists of two identical independent elements above and below the event plane. They are filled with Freon 114 with an effective length of approximately 1 m in the gas volume for the particles. Within each element, the produced light is reflected via a cylindrical and a plane mirror onto the light catcher system. These light catchers are arranged in a 2*8 matrix of the total size 20·80 cm².

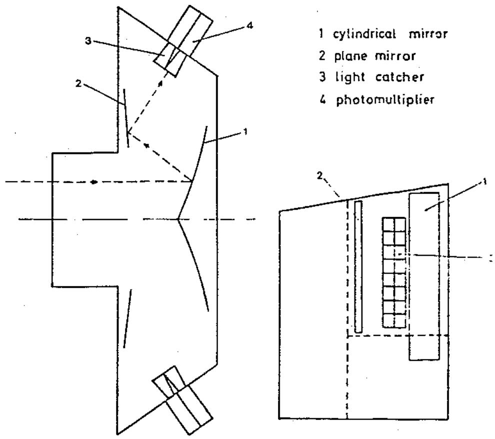

Fig.2.10: Top view and side view for the Cherenkov counters C6 and C7.

The third type of Cherenkov counter is a spherical (radius=1.2m) high pressure counters filled with Freon 114 at a pressure of 7.5 to 8.0 bar. (Fig.2.11)

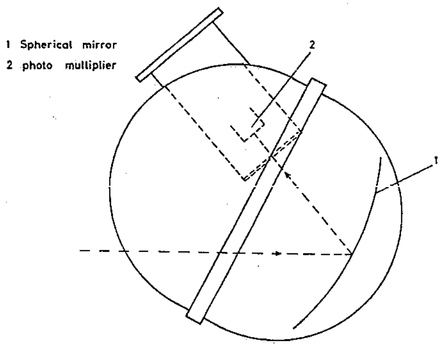

Fig.2.11: Side view of the high pressure Cherenkov.

The index of refraction is n=1.00455 with a threshold for pions of 1.45 GeV/c, 5.2 GeV/c for kaons, and 9.9 GeV/c for protons. Together with the counter C2 it was used at the 45° trigger telescope to distinguish between baryons and mesons (BRE84c).

The signals from all photomultipliers are digitized by ADC and TDC units and read out with a standard CAMAC interface.

Performance

Typical pulseheight spectra for the three types of counters are shown in Fig.2.12 not separated for the two charges. Only tracks which had a signal above pedestal have entered into these distributions. The efficiencies of the Cherenkov counters C2 and C8 have been determined using pions identified with the second counter in the same trigger telescope. It turned out that the efficiency to have a signal above pedestal for a particle which should give light, is very high and in the order of 98% to 100% dependent on the charge and the momentum of the particles (SZC82). The efficiency for the spherical high pressure Cherenkov counter (C9) is almost 100% for all charges and over the full momentum range.

The situation is more difficult for the Cherenkov counters C6 and C7 in the forward telescopes. Despite the possibility for a good spatial resolution due to the large amount of photomultipliers (16 per detector element) the efficiency depends strongly on the charge and the angle of incidence. While the efficiency is good (97%-99%) for positive particles and small polar angles ($\Theta_{LAB} \lesssim 26°$) the efficiency drops to values around 40% for negative particles at large polar angles. A large polar angle, which implies a large angle of incident, causes an increasing fraction of the light to miss the area of the light catchers and this effect is stronger for negative particles since they are bent away from the beampipe resulting in large reflection angles at the mirror planes (HER82). This is illustrated in Fig.2.13 which shows the efficiency for the counter C6 in the 20° trigger telescope for positive and negative particles as a function of the polar angle Θ_{LAB}.

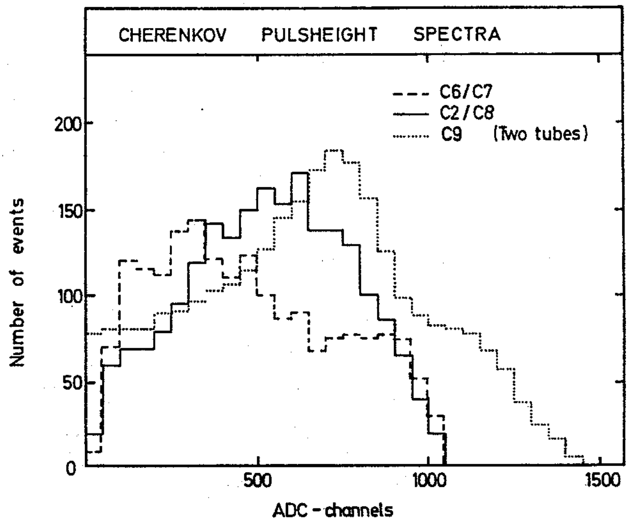

Fig.2.12: Pulseheight spectra for SFM Cherenkov counters.

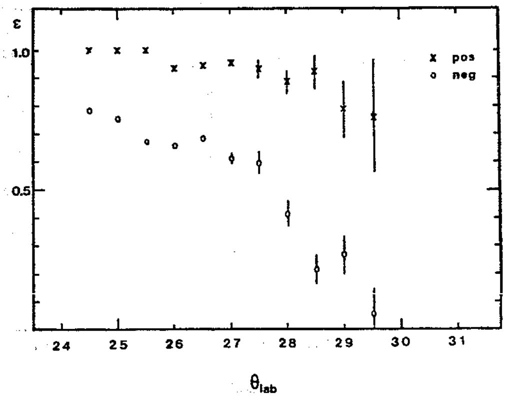

Fig.2.13: Efficiency for Cherenkov counter C6 as a function of the production angle Θ_{LAB}.

2.5 DATA ACQUISITON

After an event is accepted by the trigger system a signal is send to the data acquisition computer (PDP 11/60) which collects the data from the MWPC's and all additional devices to write it onto a magnetic tape. Standard CAMAC hardware is used to interface the computer with the experimental equipment. The following information is recorded:

- Digital information from the multi wire proportional chambers.
- Information from all analog divices digitized in ADC's and TDC's.
- Information from beam monitors and scaler information.
- ISR data from the ISR control room via the "ARGUS DATA BUS".

In addition to this data recording task the PDP 11/60 computer is used for continous monitoring of the experimental equipment. A large amount of checks performed during the setup of a new data taking period and parallel to data taking guarantees the integrity and quality of the data recorded on a tape. An immediate off-line check of at least one data tape during the first hours of a new data taking period ensures the reliability of the recorded data.

3. DATA PROCESSING

In this chapter the processing of the recorded events and the preparation of the data for the physics analysis is described..

To accomplish this task satisfactory, several requirements have to be fulfilled by the organisation of the software:

- Transportability of data and programs between several different types of computer and systems.
- Flexibility to account for changes of software and hardware (e.g. detector changes or improvements, magnetic field)
- Modularity and standardized program interfaces to allow software development by a large group of people.

The requirements on the performance of the data processing procedure are:

- Reconstruction of the complete event recorded by the spectrometer and additional devices for particle identification.
- Preparation of a Data Summary Tape (DST) which contains the information necessary for the physics analysis in a compressed form to avoid unnecessary computer resources.
- Provide a standard software framework for the physics analysis of the data to enable easy access to the data for every user.
- Possibility for the complete simulation of events and experimental equipment with the standard programs.

3.1 OFFLINE EVENT RECONSTRUCTION

The complete reconstruction of the event is performed in several steps which are described in more detail in the next sections. All events which passed the selection criteria are processed through a program chain for pattern recognition, trackfitting , the reconstruction of the primary event vertex and, if present, the reconstruction of secondary vertices. The information from additional detector elements used for the identification of the particles are treated after this geometrical reconstruction of the event. For each event the coordinates of the primary vertex and eventually of secondary vertices and the four-momenta of all reconstructed particles using all additional information from Cherenkov counters, dE/dx and time of flight measurement are written to a Data Summary Tape (DST).

3.1.1 Trackfinding and trackfitting

The geometrical reconstruction of a single track in the magnetic field is divided into three different processes. Track candidates are first found in two different projections and connected to a track in space in the second step (trackfinding) followed by the determination of the track parameters (trackfitting).

Pattern recognition in one projection

The task of this first step of the pattern recognition procedure is to find a set of clusters (trackhits, $y_i = y_1,,,y_n$) in one projection which could form a candidate for a possible track. A simple linear track model (NOR78,WIN72) was used to describe the particle trajectory. Starting at an initial track point in a chamber plane, the expected hit in the next plane is predicted with the track model using the clusters in all preceding planes. This process is started with clusters in planes far away from the vertex since the cluster density is lower than in the interaction region and the tracks are generally better separated by the magnetic field.

Are x_i (i=1,,,n-1) the coordinates of clusters in the planes 1,2,,,n-1, Then the coordinate of the expected cluster in plane n is predicted as

$$x_n = \sum_{i=1}^{n-1} a_{in} \cdot x_i$$

For a genuine track candidate the coordinate x_n is expected to fulfil the condition

$$c_{1n} < (x_n - \sum_{i=1}^{n-1} a_{in} \cdot x_i) < c_{2n}$$

where a_{in} are the prediction coefficients for plane n and c_{1n} and c_{2n} are the prediction limits for this plane and x_i are the cluster coordinates already associated with the track candidate. These coefficients as well as the prediction limits are determined by least squares fitting to a large sample of simulated tracks and implicitly contain the magnetic field. The trackfinding process is therefore a comparison with simulated tracks represented by the coefficients a_{in} and c_{in}. This accumulation process is performed only with a specific set of planes for each candidate. To allow for missing clusters (holes) in certain planes due to chamber inefficiencies, different subsets of planes are tested with different sets of coefficients and limits.

After this accumulation process the track is represented by a polynomial in the x-coordinates of the form:

$$y = \sum_{i=1}^{N_V} A_i \cdot x^{i-1}$$

for the vertical projection and

$$z = \sum_{i=1}^{N_h} B_i \cdot x^{i-1}$$

for the horizontal projection. The x-coordinates in the polynomial are usually the position of the chamber planes. The coefficients A_i and B_i are either fitted to the real track or they are deduced from linear combination of y_i and z_i in their reference planes:

$$A_i = \sum_{j=1}^{N_{vr}} C_{ij} \cdot y_j \quad \text{and} \qquad B_i = \sum_{j=1}^{N_{hr}} D_{ij} \cdot z_j$$

where N_{vr} and N_{hr} are the number of reference planes used in the vertical projection and in the horizontal projection. The coefficients C_{ij} and D_{ij} are again determined by least squares fitting to a large number of simulated tracks.

This parametrization of tracks using polynomials has two important advantages:

- The algorithm is easy and fast to calculate
- The magnetic field is not used explicitly, it is implicit to the parametrization.

Combination of track candidates to a spatial track

The polynomial representation of the track candidates together with the information from the inclined wires are used to combine two one-dimensional track candidates in space. With two track candidates, one in the x-y plane and one in the y-z plane, a spatial track can be constructed if this is not already ruled out by the geometrical constellation of the two candidates. For the tracks constructed this way the y and z-coordinates of the intersect with planes of inclined wires can be calculated using the polynomial representation of the candidates. With the wellknown angle of inclination α the address of the inclined wires can be predicted which should give a signal if the combination under consideration represents a real track in space.

A first estimation of the momentum p of the track candidate is then given by:

$$1/p = c_0 + \sum_{i=1}^{N_v} c_i \cdot A_i + \sum_{j=1}^{N_h} c_j \cdot B_j$$

The coefficients $c_0, c_1, ..c_N$ are again determined by least squares fitting to simulated tracks.

Determination of the track parameters - Trackfitting

With the track candidates found in the trackfinding process a "quintic-spline"-fit is performed to determine the track parameters (WIN73,WIN74,DRI76). A spline curve consists of polynomials which may have different orders in different intervals of the full extension of the track. The only constraint is the continuity of the polynomials and their first derivatives at the limits of the intervals. For the fitting process, a track curve r(s) is determined and compared with the observed track hits. The curve r(s) is determined by 5 parameters;

Y_0, Z_0	Two coordinates in a fixed plane, e.g. the first cluster of the track candidate.
Y', Z'	Two direction cosines at this space point (dY/ds and dZ/ds).
Q/p	The charge and the momentum of the track.

The equation of motion to connect the track parameters with the curve r(s) and the magnetic field B is:

$$p/Q \cdot d^2r/ds^2 = dr/ds \cdot B$$

One Runge-Kutta integration is performed with the starting values of the parameters. With B and dr/ds one can determine $p/Q\ d^2r/ds^2$. The second derivative d^2r/ds^2 is parametrized by a cubic spline function f_0.

After two integrations one obtains a "quintic spline" function f_2. Together with two constants, r_0 and t (starting point and starting direction), the model is linearized and has the form:

$$r(s) = r_0 + t \cdot s + Q/p \cdot f_2$$

The fit of the parameters is then reduced to an inversion of a 5x5 matrix. With the parameters obtained by the fit new values for dr/ds and B(r) are calculated and the procedure is repeated until the parameters are stable.

The output of this procedure are the five parameters and the error matrix. Multiple scattering in the chambers can produce an error of the same order of magnitude as the spatial resolution in the chambers. The error matrix is therefore modified to account for this error.

3.1.2 Vertex reconstruction

For events with more than one reconstructed track a determination of the primary event vertex is tried. Only tracks with a small error on the fitted momentum ($\Delta p/p \lesssim 0.3$) are used in this procedure. These tracks are extrapolated towards the interaction region to find a space point which minimizes the function:

$$\chi^2 = \sum_i (V - X_i)^2/\sigma_i^2$$

where X_i is the space point of closest approach of track i to the vertex V. The error on the distance $|V - X_i|$ is denoted by σ_i.

All tracks not used in this procedure are tested on the compatibility and possibly associated with the event vertex.

It should be mentioned that the reconstruction program can handle also secondary vertices due to the decay of neutral strange particles and conversions (RAU82).

3.1.3 Particle identification with Time-Of-Flight counters

After the reconstruction of the tracks in the magnetic field of the detector the charge and the momentum components of the tracks are known. To determine the mass of the particles, the information from additional detectors is used.

All reconstructed tracks are tested whether they can be associated with a signal in one of the Time-Of-Flight counters. This is done by extrapolating the track towards these counters and by a comparison with the recorded information. If they can be associated with a time signal in the scintillation counters they are input to a procedure which aims for the determination of the mass of the particles. In order to determine the time of the interaction t_0, two different methods have been used. In one case the mass of at least one particle is determined by other means, like Cherenkov counters,therefore the time of flight of this particle is known and the time t_0 can be calculated. The second treatment is a statistical method and requires a minimum number of particles with signals in the time of flight measurement system (TOF). The masses of all these particles are a priori unknown and the pion mass is assigned to these particles. The unknown parameter t_0 is calculated and determined by a least squares minimizing procedure. Details about these two methods and their performances are found in ref. (SAJ80).

3.1.4 Particle identification with dE/dx counters

Another possibility for the identification of particles is the measurement of the energy loss in two dE/dx-chambers. While the digital information (the wire address) from these chambers is already used in the track reconstruction, the analog information can be used for an assignment of the particle mass. A detailed description of the analysis and the performance for these devices is given in reference (HEI82).

3.1.5 Particle identification with Cherenkov counters

The identification of the triggering particle with large transverse momentum is performed using the gas-filled threshold Cherenkov counters described in section 2.2.5. After the geometrical reconstruction the trigger track is extrapolated towards the appropriate Cherenkov counter and tested whether it traverses the counter through the entrance window (active area of the counter) and possibly could give a light signal at the photomultipliers. In this case the information from the Cherenkov counter (light or no light) together with the reconstructed particle momentum is used to distinguish between different mass hypothesis and, if possible, to associate a unique mass to the trigger particle. For two types of Cherenkov counters an additional treatment is necessary.

For the high pressure ball Cherenkov the path of the particle through the device is reconstructed and the total pathlength is calculated and recorded to get a better estimation about the possible production of light in the counter. For inclusive cross sections a cut is applied on this pathlength to assure a high efficieny of the detector (LOH85).

The small Cherenkov counters in the two forward trigger telescopes around 10° and 20° have a better spatial resolution than all other counters because of the large number of phototubes (32) in each counter. Since the particle density in the forward telescopes is rather high, it is not unusual that more than one particle passes through the active area of the counter. One has to make sure that the right particle is associated to a signal from a phototube. For all particles passing through the entrance window of the counter an appropriate "light cone" consisting of a finite number of "photons" is generated and these simulated photons are tracked through the detector. In such a way one can determine those phototubes which should have given a signal in case the particle has produced light on its way through the gas of the Cherenkov counter. Only the information from those tubes predicted by the simulation are used for the later analysis. To illustrate the performance of this "ray tracing" procedure, a comparison between the prediction and the measured signals is shown in Fig.3.1: The figure shows a typical distribution of the difference between the centre of the predicted light cone at the plane of the photomultiplier matrix and the reconstructed centre of the coordinates of those phototubes with a signal above pedestal.

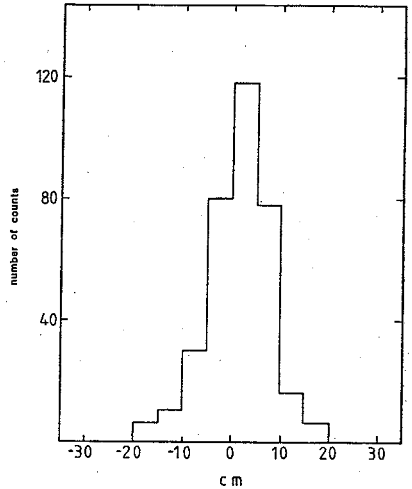

Fig.3.1: Difference between predicted and measured signals at the photomultiplier matrix.

The information from the Cherenkov counters which is entered into the DST consists of the spatial information, the ADC-values, and a mass hypothesis for the particle.

3.1.6 Organisation of the reconstruction program

The reconstruction of the complete event is performed in several steps:

- preparation of the raw data for reconstruction, like initialisation, wire address decoding, setting up of detector and calibration constants.

- trackfinding and trackfitting without vertex
- vertex reconstruction.

- trackfinding with vertex and trackfitting without vertex.
- vertex reconstruction, possibly with more tracks than before.

- trackfinding and trackfitting with vertex.
- test on vertex compatibility for remnant tracks.

- trackfit for tracks not associated with the vertex or with large momentum uncertainties using the vertex as an additional space point.

- reconstruction of secondary vertices.

- treatment of additional information from devices for particle identification (TOF,dE/dx,Cherenkov)

3.2 ORGANISATION OF THE DATA PROCESSING

The processing of the recorded data proceeds in several steps. In the first step, as it was described in the last section, the trigger track is reconstructed and only events which passed certain selection criteria on the trigger particle are passed to the program chain for the full event reconstruction in the second step. A final step reduces the available information to those quantities needed for the physics analysis producing a Data Summary Tape (DST).

The program packages PATCHY (KLE83) and HYDRA (BOC81) are used for the organisation of the programs and the data and to provide good transportability of programs and data between different types of computers and systems. The analysis has been performed at IBM,VAX,NORD,CDC, and MODCOMP computer installations.

3.2.1 Data Reduction and Event Selection

In order to reduce the computer time needed for the event reconstruction (about 15 sec for the reconstruction of one complete event on a IBM 370/168) all events are processed through a fast selection procedure. The track reconstruction and fitting is performed only in a region limited to the region of the triggering large p_T particle in order to reconstruct the triggering particle. Only those events are used in the further analysis where a large p_T particle was found and successfully reconstructed. Additional selection criteria, for example a cut on the transverse momentum of the large p_T particle, can be used for a further reduction of the data sample. This selection has been performed on a set of 168/E hardware processors (KUN76) which have almost the same instruction set as the IBM 370/168.

3.2.2 Data statistics

trigger at:	events:	events after selection:	events on DST:
10°	≈ $8.0 \cdot 10^6$	≈ $1.4 \cdot 10^6$	482287
20°	≈ $2.7 \cdot 10^6$	≈ $1.0 \cdot 10^6$	224234
45°	≈ $1.1 \cdot 10^7$	≈ $5.5 \cdot 10^5$	135143

The data were taken between September 1981 and May 1983. Part of the data with large p_T triggers at 45° were taken in 1978 with a slightly different experimental setup. The selection was done at CERN and the full reconstruction was performed at CERN, at the Institut für Hochenergiephysik in Heidelberg and at the Universität Dortmund.

3.3 EVENT SIMULATION AND ACCEPTANCE CALCULATION

The necessity for a simulation of events or tracks in the detector was already mentioned in previous sections on event reconstruction. The applications for these simulations are:

- Determination of constants for the reconstruction and test of the reconstruction program.
- Design of hardware.
- Acceptance calculation for single tracks.
- Determination of acceptance and detector resolution for exclusive reactions (e.g. decays, resonance production).

3.3.1 Detector simulation

The simulation program (MES78) can trace particles through the magnetic field of the detector and calculate the intercept of the particle trajectories with the planes of the multiwire proportional chambers. These coordinates are transformed into addresses of wires and those can be used as input to the standard reconstruction program chain. The multiple Coulomb scattering, energy loss, absorption, bremsstrahlung pair creation, and decays of unstable particles and resonances are included in this simulation process and properly taken into account.

3.3.2 Acceptance calculation

Simulation and reconstruction

The measured inclusive particle spectra are a convolution of the "real" distributions with the acceptance and the momentum resolution functions. To determine these "real" distributions the measurement has to be corrected for these effects. To determine these acceptances, which should implicitly contain the momentum resolution, a large sample of single particles have been generated with distributions very close to the physical reality. From a vertex generated according to measured distributions, these particles are tracked through the detector with the program as mentioned in chapter 3.3.1. Since only single track events have been generated for the acceptance calculation, a special treatment has to be applied for the vertex handling in the reconstruction. In the first step of the reconstruction, the tracks are reconstructed as usual without a vertex, but no primary vertex can be determined with a single track. For the following steps in the procedure, where usually the recon- structed vertex is used for the trackfinding and trackfitting process, the generated vertex is used with some displacement according to experimentally determined uncertainties on the reconstruction of the vertex coordinates (RAU82, REN85). This method simulates the influence of the vertex on the reconstruction efficiency very well and is much faster and easier than the complicated and time consuming simulation of complete events.

Acceptance correction

All measured distributions $g(\Omega')$ have to be corrected for the combined detection and reconstruction inefficiencies as well as for the finite momentum resolution to get the "real" distribution $f(\Omega)$. Between $g(\Omega')$ and the true distribution $f(\Omega)$ the following relation holds:

$$g(\Omega') = \int f(\Omega) \cdot h(\Omega-\Omega')\, d\Omega$$

where $h(\Omega-\Omega')$ is the probability to measure a particle in the phase space interval $\Omega' \cdot d\Omega'$ which originated at Ω.

The acceptance is determined with the method described above as:

$$\varepsilon = \int N^{gen}(\Omega) \cdot h(\Omega-\Omega')d\Omega / N^{gen}(\Omega')$$

$$= N^{rec}(\Omega')/N^{gen}(\Omega')$$

where $N^{rec}(\Omega)$ and $N^{gen}(\Omega')$ are the known densities of reconstructed and generated tracks in the phase space interval $\Omega' d\Omega$.

With this definition, the acceptance can exceed one. It looks peculiar that the detection efficiency is larger than 100%, but it has the advantage that the momentum shift due to the finite resolution is automatically taken into account. Every track is than weighted with the inverse value of the acceptance ε which is available as a function of y, ϕ, p_T and the charge of the particle. The statistical error on the calculated acceptance is generally lower than 5% except the regions with very low acceptance (below 0.08) where the relative error exceeds 20%. All inclusive distributions shown in this analysis are corrected for acceptance losses using the efficiency determined with the method described above.

4. PARTICLES WITH LARGE P_T IN THE PARTON MODEL

4.1 THE PARTON MODEL

The first experiments at energies high enough to observe characteristic features of deep inelastic scattering gave a strong impact on the evolution of our current picture about the structure of matter. Experiments on deep inelastic electron nucleon scattering (BLO70,MIL72) are basically described by two dimensionless structure functions, W_1 and W_2. It was shown that both structure functions are asymptotically independent of the momentum transfer Q^2 between the lepton and the nucleon for asymptotic values of Q^2.

$$W_{1,2}(Q^2,x) \rightarrow F_{1,2}(x) \quad \text{for large } Q^2.$$

with $x = Q^2/2p\cdot q$, where p is the initial parton momentum and q the momentum of the exchanged photon.

This behaviour is called the "Bjorken scaling" of the structure functions and was predicted by Bjorken (BJO69a) before it was supported by the experiment.

This approximate scaling behaviour can be explained in a model in which all hadrons are composed of independent, pointlike, and non-interacting constituents, the partons (FEY69). At large momentum transfer, Q^2, the virtual photon in deep inelastic electron nucleon collisions is assumed to scatter incoherently off a beam of quasi free partons. The electromagnetic interaction between electrons and nucleons is then described by the interaction of the electron with one quasi free parton inside the nucleon. The variable x is identified to the fraction of the nucleons momentum carried by the struck parton before the interaction. It was a natural step forward to combine this parton model with the quark model (GEL64,ZWE64) and the colour SU(3) model (FRI73) which was successfully used in hadron spectroscopy (ABR64) and to identify the partons to coloured quarks. The open question was the interaction of partons and it was tried to formulate a theory based on the quark parton model and the principle of gauge invariance.

A field theory based on non-Abelian, local gauge invariance was the result of these attempt: Quantum Chromodynamics (QCD). For the formulation of the theory see e.g. (FRI73,POL73). The interaction in this theory is mediated by coloured gluons which, together with the quarks, are constituents of the hadrons and thus carry part of their momenta. The gluons and their interactions are the reason for the approximate scaling behaviour which, in their absence, would be exactly fulfilled. Since in QCD, in contrast to Quantum Electrodynamics (QED), both, quark and gluons carry colour charge, the gluons can couple which each other through a triple gluon vertex (GLU81). This results in a vacuum polarization totally different from that in QED and therefore in a different Q^2 dependence of the strong coupling constant α_s in QCD. The theory predicts that the coupling constant decreases as the momentum transfer Q^2 increases and falls to small values at very large values of Q^2: non-Abelian gauge theories are asymptotically free. Asymptotic freedom provides a qualitative understanding of the scaling behaviour in deep inelastic processes at asymptotic values of Q^2. Unfortunately there are still problems and open questions in this theory. Calculations in field theories are normally performed using perturbative techniques. This works very well in QED since the coupling constant is very small hence the contributions from higher orders vanish rapidly. In QCD the coupling constant α_s gets larger when Q^2 is small and perturbation techniques do not work easily. Confident calculations can only be performed for processes with large Q^2. This was done for $e^+ e^-$ annihilation into hadrons, Drell-Yan mechanisms and especially deep inelastic lepton-nucleon scattering where QCD was most successful to correctly describe the small scaling violation effects at finite values of Q^2 (BUR78). Another open question is the fact that no free quarks or gluons have been observed and a complete theory should be able to account for this confinement problem. Despite these problems, QCD appears to be the best candidate for a theory which describes strong interactions.

4.2 DISTRIBUTION OF THE PARTONS IN THE INITIAL PROTONS

4.2.1 Longitudinal distribution of the partons

Electron-nucleon scattering

As already mentioned, the structure of the protons for electron nucleon interactions is described by two dimensionless functions $F_1(x)$ and $F_2(x)$ measuring the longitudinal distributions of quarks inside the protons.

If $f_i(x)$ is the probability for finding a quark of type i with a momentum fraction x, then:

$$2 \cdot x \cdot F_1(x) = F_2(x) = \Sigma\ z_i^2 \cdot x \cdot f_i(x)$$

where z_i is the charge of a type i quark.

Between the functions $F_1(x)$ and $F_2(x)$ a simple relation holds, dependent on the spin of the partons (CAL69):

$$F_1(x) = 0 \qquad \text{for spin 0 partons}$$

and $$2 \cdot x \cdot F_1(x) = F_2(x) \qquad \text{for spin 1/2 partons}$$

The experimental results support the hypothesis that the charged partons have spin 1/2. Considering lepton-nucleon interactions, the charged partons can be classified into two groups, the valence quarks $q_v(x)$, responsible for the quantum numbers of the proton, and the sea quarks, $q_s(x) + \bar{q}_s(x)$, for which we assume that the quark and antiquark distributions are the same.

Momentum conservation requires

$$\int_0^1 dx \sum_i x \cdot f_i(x) = 1 - \varepsilon$$

where ε is the fraction of the total momentum carried by neutral partons or gluons. The experiment (STE75) suggests that about 50% of the nucleon momentum is carried by gluons.

Neutrino-nucleon scattering

Another possibility to probe the structure of the nucleons is to study interactions of ν or $\bar{\nu}$ with nucleons. The cross section for neutrino-nucleon scattering is much smaller than that for electron-nucleon scattering but it offers the possibility to distinguish between different quark flavours in the scattering process: in charged current interactions, neutrinos only couple to negatively charged valence quarks or sea quarks, and antineutrino only couple to positively charged quarks. A third structure function, $F_3(x)$, has to be introduced to describe neutrino-nucleon scattering due to the V-A coupling of weak interactions. The relation

$$F_2^{eN} = 5/18 \cdot F_2^{\nu N}(x)$$

can be derived from the quark parton model where the factor 5/18 represents the average charge squared of the quarks inside the nucleon taking the average over protons and neutrons. This relation is fulfilled to a good approximation (MUS78).

A measurement of the x-distribution from both ν and $\bar{\nu}$ scattering offers the possibility to determine the quark and antiquark distribution functions separately. The gluon distribution function can be determined using the Altarelli - Parisi evolution equations (ALT78), a system of integro-differential equations relating the gluon and quark distribution functions. An example for the distribution functions $f_i^{\nu N}(x)$ for gluons, valence quarks and sea quarks is shown in Fig.4.1 (BER83).

It turns out that only valence quarks are found at large x. The observed scaling violations, appearing as a Q^2 dependent structure function $F_2^{\nu N}(x,Q^2)$, are

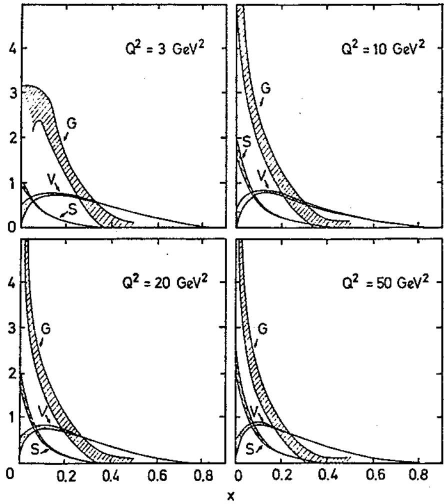

Fig.4.1: Distribution functions for gluons (G), valence quarks (V) and sea quarks (S) for different values of Q^2.

due to gluon bremsstrahlung inside the protons and this "scale breaking" is implicitly contained in the Altarelli-Parisi equations (KOG74,ALT77). A schematic view of this gluon bremsstrahlung mechanism is shown in Fig.4.2.

4.2.2 Transverse motion of the partons - primordial k_T

The scale breaking of the structure functions has some impact on the transverse structure of the protons. A simultaneous measurement of $F_1(x)$ and $F_2(x)$ shows a clear deviation from the naive expectation from the Callan-Gross relation (CAL69) at low values of x (ABR83,BER84). This deviation can be interpreted as the contribution of finite transverse momenta of the partons in the nucleons. Partons as a bound system with a finite transverse extension are expected to have a transverse momentum k_T of about 300 MeV/c due to the Heisenberg uncertainty principle. In Quantum Chromodynamics one expects to obtain an additional transverse momentum of the partons due to gluon bremsstrahlung before an interaction with leptons or other partons which is responsible for the "scale breaking" of the proton structure functions. The mean

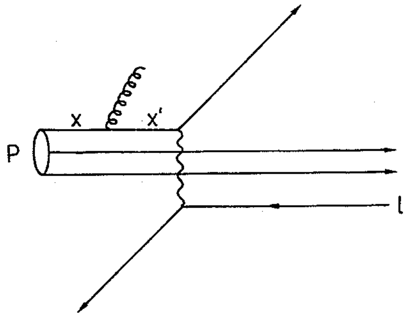

Fig.4.2: Schematic view of intrinsic gluon bremsstrahlung in deep inelastic lepton-nucleon collisions. Incoming proton (P) is probed by a lepton (l) Bjorken x' seen by the lepton not equal "real" x.

value of this "perturbative k_T" is expected to depend on the x values of partons and the Q^2 of the interaction process. The observed, "effective", transverse momentum, k_T, is a superposition of these two different sources. The perturbative constituent transverse momentum can be directly observed in the Drell-Yan process $pp \rightarrow \mu^+\mu^- + X$ (HOM76) leading to rather high values for k_T of about 800 MeV/c (FEY78). Experiments with particles at large transverse momentum measuring the momentum distribution perpendicular to the event plane indicate that the mean value of k_T must be higher than 500 MeV/c (DEL77).

A detailed analysis of these effects and a measurement of k_T has been performed at the ISR and reported in reference (GES86).

4.3 DEEP INELASTIC HADRON-HADRON SCATTERING

In hadron-hadron interactions at high energies most of the available energy is taken by particles moving in the direction of the incoming hadrons with limited transverse momenta of the order $\langle p_T \rangle \approx 0.3$ GeV/c. Sometimes, however, particles are produced with unusually large transverse momenta (ALP73, BAN73, BUE73). After this has been found, it was speculated that these particles arose from an exceptionally hard collision between the constituents of the incoming hadrons.

4.3.1 The basic process

The process where large transverse momentum particles are produced is assumed to occur as the result of a mechanism illustrated in Fig.4.3.

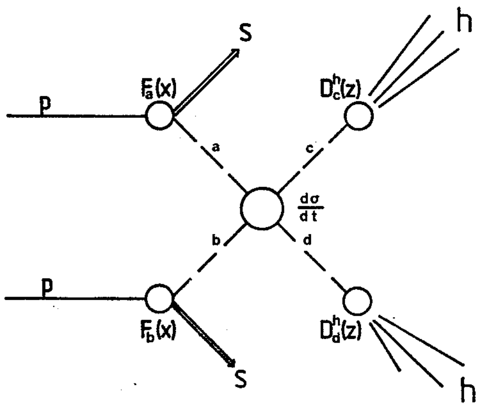

Fig.4.3: Schematic representation of the scattering process. Two partons (a,b) are scattered out of the incoming protons (p) leaving behind a spectator system (s). The fragmentation of the scattered partons into hadrons (h) ist indicated.

Three independent ingredients describe the process. Before the interaction, the partons inside the incoming hadrons are described by structure functions $F(x,Q^2)$ which include the longitudinal and transverse motion of the constituents. The interaction is described by the parton-parton differential cross section $d\sigma/dt$ calculated in a first order perturbative QCD calculation. The scattering process is followed by the hadronization or fragmentation of the scattered partons and the hadron remnants into observable particles. The fragmentation process is described by fragmentation functions $D^h_q(z)$. The fragmentation function $D^h_q(z)$ gives the probability that a parton of type q fragments into a hadron of type h, with a fraction z of the original longitudinal momentum of the parton.

4.3.2 Parton-parton differential cross section

The differential cross section for parton-parton scattering can be written as:

$$d\sigma/d\hat{t} = \pi\cdot\alpha^2_s(Q^2)\cdot|A|^2/\hat{s}^2$$

where $\hat{t},\hat{s}$ are the usual Mandelstam variables in the parton parton rest system and $\alpha^2_s(Q^2)$ is the Q^2 dependent, running coupling constant. The matrix element $|A|^2$ can be calculated in first order QCD for all different subprocesses (COM77).

The effective strong interaction coupling constant in the QCD leading log approximation has the form:

$$\alpha_s(Q^2) = g^2/4\pi = 12\ \pi/((33-2n_f)\cdot(\ln(Q^2/\Lambda^2)))$$

where n_f is the number of active quark flavours, g the strong coupling constant and Λ an unsatisfactorily determined scale factor that could be evaluated from the amount of "scale breaking" observed in the experiment. The analysis of the scale breaking in lepton-nucleon collisions indicates that Λ is in the range 0.3-0.7 GeV/c (e.g. BUR77, BUR78). For lepton-nucleon collisons, Q^2 is the four momentum transfer from the lepton to the interacting parton. For the process indicated in Fig.4.3 the value of Q^2 is not known and in model calculations the definition:

$$Q^2 = 2\ \hat{s}\cdot\hat{t}\cdot\hat{u}/\ (\hat{s}^2 + \hat{t}^2 + \hat{u}^2)$$

is a possible choice (FEY78), where $\hat{u},\hat{s},\hat{t}$ are the usual Mandelstam variables in the rest system of the interacting partons.

4.4 HADRONIZATION OF PARTONS INTO OBSERVABLE PARTICLES

After the short discussion of parton-parton scattering, one has now to ask the question how the scattered quarks, gluons or hadron remnants turn into observable hadrons. The theoretical picture in QCD assumes quarks and gluons to carry a quantum number called "colour" while observable particles are colourless. The coupling constant $\alpha_s(Q^2)$ increases to infinity if $Q^2 \rightarrow 0$, leading to "confined" partons (see e.g. REY79). In a naive picture this could work as follows: when two coloured objects are pulled apart, the forces responsible for the confinement build up a colour field between the partons (Fig.4.4a). The strength of this field is increased when two partons move apart (Fig.4.4b) until a quark-antiquark pair is created because this is energetically favoured and breaks the field (Fig.4.4c).

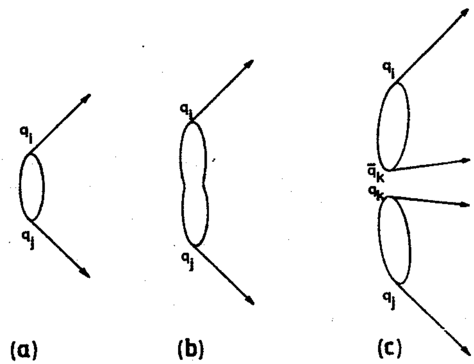

Fig.4.4: Colour field stretched between propagating partons.

The quarks and antiquarks produced now gather into colour singlets ($q\bar{q}$ and qqq) forming mesons and baryons.

The dynamics of this process is described by a fragmentation functions $D^h_q(z)$. The fragmentation function $D^h_q(z)$ is a measure for the probability that a parton of type q fragments into a hadron of type h with a momentum z·p, where p is the momentum of the fragmenting parton. For the present these functions are supposed to be a function of z only, thus showing a scaling behaviour. The fragmentation functions are normalized such, that:

$$\sum_h \int_0^1 D^h_q(z)\cdot z\cdot dz = 1$$

The fragmentation functions are assumed to be independent of how the parton q was produced and of its colour. This fragmentation process can not yet be calculated by QCD and some phenomenological parametrizations for hadron production have to be used instead. Since they do not depend on the origin of the parton, they could be determined from electron-positron annihilations by studying the hadron spectra. As for the structure functions, scaling is violated due to final state gluon bremsstrahlung effects leading to Q^2 dependent fragmentation functions (e.g. ING84):

$$D^h_q(z) \rightarrow D^h_q(z,Q^2)$$

This was confirmed experimentally in e^+e^- annihilation experiments (e.g. BRA82c). An example for several quark fragmentation functions as derived from electron positron annihilations (DAK74) are given in Fig.4.5.

4.4.1 Non-perturbative models

In this section the two most widely used fragmentation schemes are examined. Two purely phenomenological parametrizations known as the Feynman-Field model (FIE77, FIE78b) and the LUND model (AND79a).

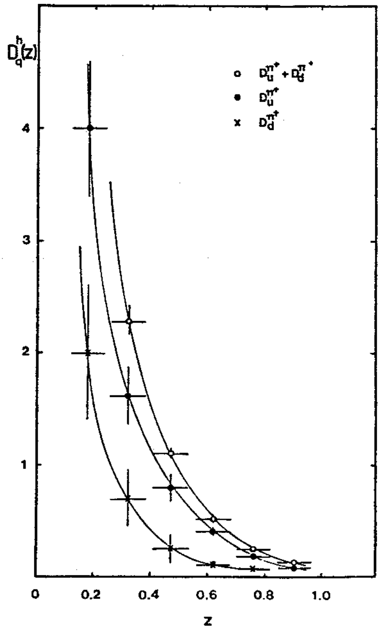

Fig.4.5: Fragmentation functions for quarks, derived from electron positron annihilations (DAK74).

The Feynman-Field quark jet model

The Feynman-Field (FF) model is a parametrization for hadron production and the qualitative features are neither "derived" nor "explained" by the model. An illustration of quark jet fragmentation in the Feynman-Field scheme is shown in Fig.4.6

In the colour field a quark-antiquark pair is created to form a hadron h_1 of rank one together with the initial quark. The remnant quark forms a hadron h_2 of rank two together with another antiquark from a created quark-antiquark pair. The energy sharing between the quark and the meson is described by a probability function f(z) where z is the fraction of the total energy of the quark of rank n which is taken by the meson of rank n. This probability function f(z) and the resulting fragmentation function for the produced hadrons are related by the integral equation:

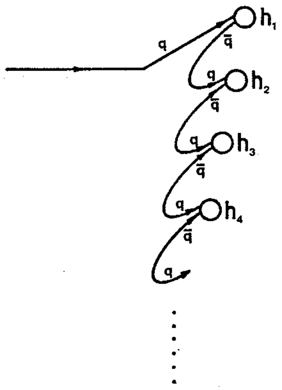

Fig.4.6: Feynman-Field fragmentation scheme for quarks.

$$D(z) = f(z) + \int_z^1 d\eta \cdot (f(1-\eta) \cdot D(z/\eta))$$

The function f(z) is parametrized as:

$$f(z) = 1 - a + 3a \cdot (1-z)^2$$

with the parameter a. Two additional features of the Feynman-Field parametrization should be mentioned here.

An extension of the model concerns the fragmentation of gluons. In the models from Ali (ALI80) and Hoyer (HOY79), the gluon is hadronized by first splitting them into a quark-antiquark pair or a single quark followed by quark fragmentation using the standard Feynman-Field scheme. As a consequence, gluons have a steeper fragmentation function, and gluon jets are "softer" than quark jets.

The production of baryons with three quarks is performed by creating a diquark and a antidiquark, requiring the introduction of an additional parameter: the probability to create a diquark - antidiquark pair from the vacuum. The fragmentation chain is stopped when the remaining quark is sufficiently soft, i.e. the mass one could produce is lower than the mass of the pion. A typical value of E ≈ 1GeV is used to terminate the cascade.

The LUND model

The LUND string fragmentation model is a simple picture for the hadronization of a colour field stretched between two coloured objects (AND79a, AND79b, AND80). The LUND model is slightly different from the Feynman-Field model. The Feynman-Field model involves independent fragmentation of the quarks, while in the LUND model the pair production is a result of the confining force between the coloured objects and fragmentation describes the evolution of the entire system. A socalled "string" is stretched between two separating quarks (colour triplets) (Fig.4.7) which breaks up when the colour forces become too strong (SJO82).

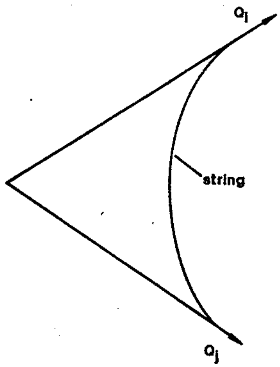

Fig.4.7: LUND string stretched between separating quarks.

The created quarks and antiquarks then link with the original quarks to produce individual colourless systems. A snapshot of the space-time evolution of a string between two quarks and the breaking up into quarks and antiquarks is displayed in Fig.4.8.

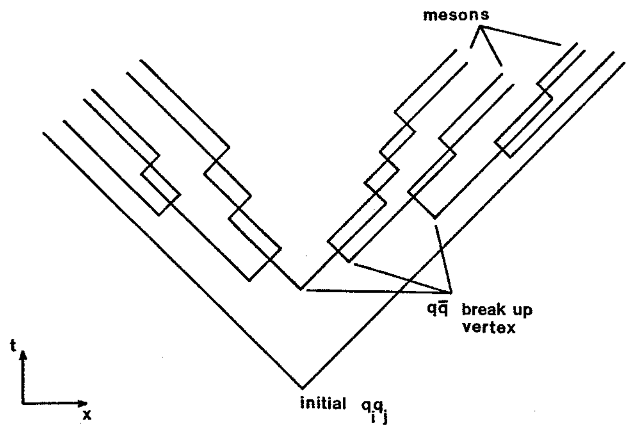

Fig.4.8: Breakup of a string and formation of hadrons in the LUND fragmentation picture.

The dynamical description of the fragmentation is physically motivated by a "tunneling process" leading to a form for the function f(z) like:

$$f(z) = (1+c)\cdot(1-z)^c \quad (\text{with } c \approx 0.3\text{-}0.5)$$

Gluons in the LUND model appear as "kinks" in a quark-quark string as illustrated in figure 4.9 for the process $e^+e^- \rightarrow q\bar{q}g$.

The gluon is always coupled to two strings because the gluon is a colour octet and carries colour and anticolour. It is therefore not necessary to introduce additional assumptions on gluon fragmentation like in the Feynman-Field model since a string system involving gluons is hadronized in the same way as a single

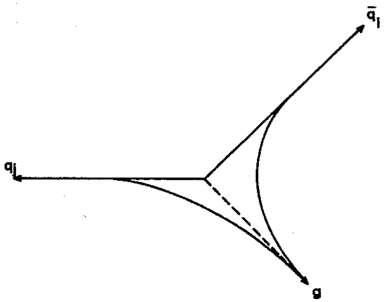

Fig.4.9: Representation of a gluon in the LUND string picture for e^+e^- annihilations into quarks.

string. Since the energy of a gluon is shared between two strings, gluon jets are generally softer than quark jets in this fragmentation model.

Baryons in the LUND model are produced by creating a diquark and an antidiquark in the colour field. The probability to create such a diquark antidiquark system is an additional parameter in the model.

4.4.2 Perturbative models

In the leading-log approximation to perturbative QCD, the evolution of coloured partons can be treated as a probabilistic branching process (FOX80). This is illustrated in Fig.4.10.

A quark emitting gluons results in a parton shower evolution and forms massive colourless objects ("clusters") (BAS79, BAS80, FOX80). The emission of gluons is described by first order QCD and has therefore more the features of a physical model than the non-perturbative models. Unlike the LUND and the Feynman-Field model, the QCD shower models do not require fragmentation functions or tunneling form factors. The dynamics is described by the pertur-

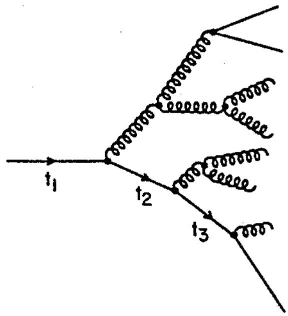

Fig.4.10: Shower evolution of a propagating quark.

bative process and the actual hadronization of clusters into hadrons is not so important and usually described using statistical and phase space parametrizations. The shower process , as illustrated in Fig.4.11, is pushed forward until the mass squared cutoff t_c is reached.

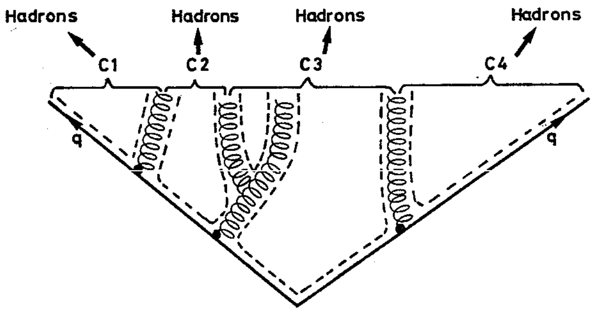

Fig.4.11: Shower process with the formation of hadrons.

Together with the leading log QCD scale Λ this is the only parameter in QCD cluster models. From e^+e^- collisions a value of t_c=2.56 GeV² is found to be a reasonable mass squared cutoff. Two similar models are used in model calculations: the Field-Wolfram model (FIE83) and the model from Webber and Marchesini (WEB83). The only difference is a slightly modified shower model and a better treatment of lighter quarks in the Webber model. Since perturbative models are not yet used for the simulation of events with a large transverse momentum particle, these models are not described in more detail.

4.5 EXPERIMENTAL EVIDENCE FOR HARD HADRONIC COLLISIONS

The hard scattering of hadron constituents in pp or pp collisions and their subsequent fragmentation into observable particles, as described in the last two sections, should result in the production of particles with large transverse momentum with respect to the incoming particles.

Along with this production of high-p_T particles, the existence of jets was predicted (BER70, BER71, ELL74), appearing as bundles of particles close together in phase space and moving in the direction of the scattered partons.

4.5.1 Single particles with large transverse momentum

From experiments performed below the ISR energies an exponential drop of the invariant cross section $Ed^3\sigma/dp^3 \propto \exp(-6p_T)$ corresponding to glancing collision of nucleons was established in the range $p_T \lesssim 1.0$ GeV/c (ALP75). It was the merit of the CERN ISR to observe a deviation from this exponential law. First results on extraordinarily high production cross section at high-p_T have come from several experiments studying pp collisions at the ISR (ALP73, BAN73, BUE73). These data were consistent with a p_T dependence like:

$$E \cdot d^3\sigma/dp^3 \approx p_T^{-N} \cdot (1-x)^M \quad \text{mb}/(\text{GeV}/c)^2$$

where N=8.6 and M=10.6

If the proton constituents are pointlike quarks or gluons, then simple dimensional counting arguments (BRO73,MAT73,SIV76) suggest that the invariant cross section scale as p_T^{-4}.

The predicted scaling behaviour of the invariant cross section:

$$E \cdot d^3\sigma/dp^3 = F(\sqrt{s}, x_T) \rightarrow s^{-n/2} \cdot F(x_T)$$

$$(\text{where } x_T = 2 \cdot p_T/\sqrt{s})$$

has been tested at the CERN ISR. If the scaling concept works, then n is a constant, if it breaks down, then n is a function of $\sqrt{s}$ and x_T. Experimental data (CLA78,ANG79) have shown that n is a function of x_T and $\sqrt{s}$ approaching the QCD prediction of n=4 at large values of x_T.

4.5.2 Four jet structure in high-p_T events

After the hard scattering of constituents had been established at the CERN ISR observing the unexpected large cross section for high-p_T particles, experiments at the ISR have reported on enhancements of particle density in the region of phase space surrounding the high-p_T particle (BUE75,BUE76,DEL75,DEL76,DEL77). Strong positive correlations in azimuth, rapidity and in transverse momentum have been observed as well as a second enhancement opposite in azimuth to the large p_T particle. These two "jets" of particles originate from the two scattered partons. Two longitudinal jets, the "spectator jets" are fragments of the two parton systems which did not participate in the hard scattering process. The secondaries in the spectator jets are believed to be approximately distributed like secondaries in normal inelastic events.

In Fig.4.12 the particle density as a function of rapidity for three different trigger momenta p_T > 2,4 and 6 GeV/c is shown as measured by this experiment (BRE84b) around $\Theta^{tri} \approx 45°$.

The rapidity of the trigger particle is indicated by an arrow. The trigger particle is not included in these distributions. Both transverse jets are expected

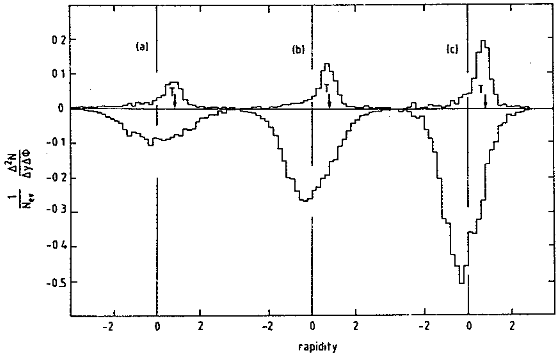

Fig.4.12: Particle density as a function of rapidity for three different trigger momenta $p_T > 2$, 4 and 6 GeV/c (a-c) and $\Theta^{tri} \approx 45°$. Particles included have $p_T > 1$ GeV/c.

to be found in the scattering plane which can be approximated by a plane defined by the trigger particle and the incoming protons. The away jet should therefore show up around $\phi = 180°$ and the trigger jet around $\phi = 0°$. Particles in the azimuthal region near the trigger particle $\phi^{sec} = \phi^{tri} \pm 25°$, "towards", are plotted upwards. Those particles opposite to the trigger at $\phi^{sec} = (\phi^{tri} + 180°) \pm 25°$, "away", are plotted downwards. All particles included in this figure have transverse momenta above 1 GeV/c. A clear enhancement of particle density is observed around the trigger region appearing as the socalled "towards jet". Opposite in azimuth the "away jet" shows up as an increase in particle density. The longitudinal spectator jets are not visible in this figure. The reason for the different appearance of the trigger jet and the away jet is the condition of a leading particle imposed on the trigger jet which decreases the available energy and approximately fixes the polar and azimuthal angle of the trigger jet. Another way of presenting the appearance of two transverse jets is used in Fig.4.13 where the relative increase of particle density with respect to normal inelastic events as a function of rapidity y and azimuthal angle ϕ for different intervals of the transverse momenta of the secondaries is plotted.

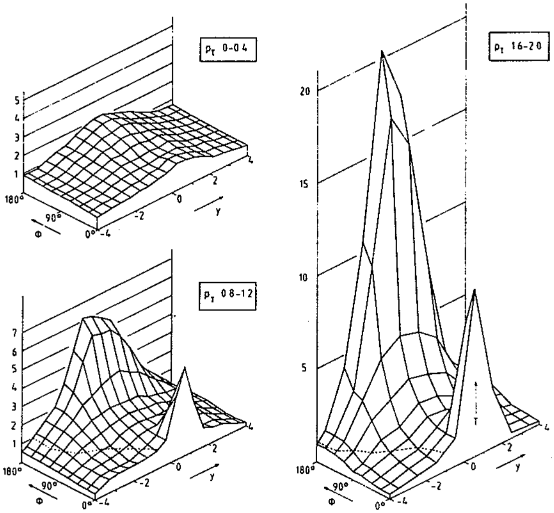

Fig.4.13: Relative increase of particle density with respect to normal events as a function of rapidity y and azimuth ϕ.
The dashed line indicates unit ratio.

The trigger particle is not included in the figure. Again a clear two jet structure is evident.

Similar plots as in Fig.4.12 for $\Theta^{tri} \approx 45°$ are plotted in Fig.4.14 and Fig.4.15 for polar angles of $\Theta^{tri} \approx 20°$ and $\Theta^{tri} \approx 10°$ respectively. The same behaviour can be observed for these different production angles: An increase of particle density in the neighbourhood of the trigger particle and opposite in azimuth.

The size of the towards jet is significantly smaller for production angles in forward directions. This is well understood since, at fixed transverse momentum of the trigger particle, the fraction of the total trigger jet momentum carried by the trigger particle increases with decreasing polar angle from values around 70% for $\Theta^{tri} \approx 45°$ to values up to 90% for $\Theta^{tri} \approx 10°$.

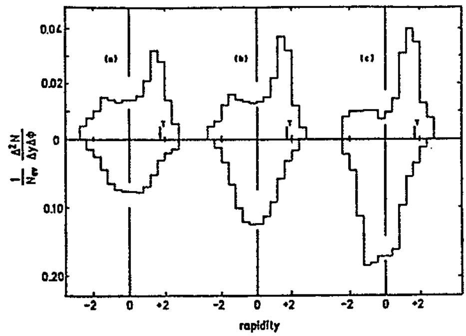

Fig.4.14: Particle density as a function of rapidity for three different trigger momenta $p_T > 2$, 3 and 4 GeV/c (a-c) and $\Theta^{tri} \approx 20°$. Particles included have $p_T > 1$ GeV/c.

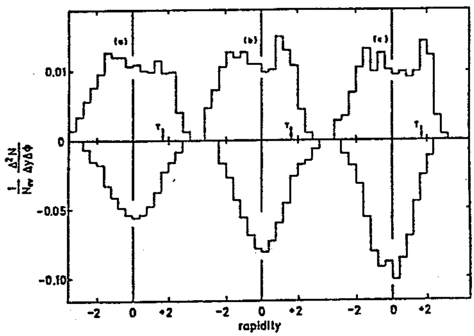

Fig.4.15: Particle density as a function of rapidity for three different trigger momenta $p_T > 2$, 3 and 4 GeV/c (a-c) and $\Theta^{tri} \approx 10°$. Particles included have $p_T > 1$ GeV/c.

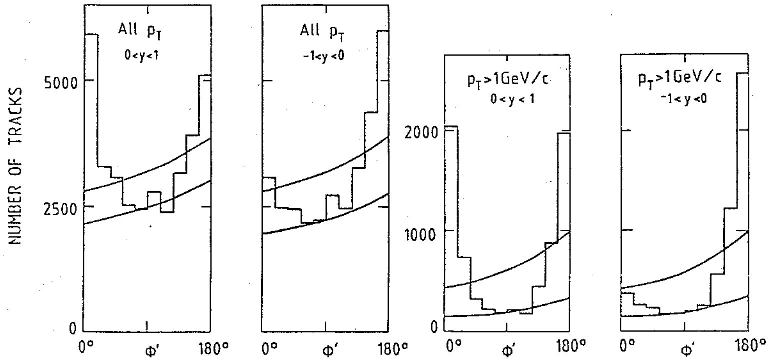

Fig.4.16: Azimuthal angle distribution for different cuts in the transverse momentum and rapidity. The solid curves are predictions from a LPS model.

The distributions of secondaries in azimuthal angle ϕ are shown in Fig.4.16 for all secondaries and for secondaries with $p_T \geq 1.0$ GeV/c for limited range in rapidity. The trigger particles, not included in the distributions, define $\phi = 0°$. Results from a longitudinal phase space model are included for two different normalization (BRE84b). One of them is normalized to the integral of the distribution, the other one to $dn/d\phi$ at $\phi = 90°$. The data show a clear peak at $\phi = 0°$ corresponding to the towards jet and another peak at $\phi = 180°$, corresponding to the away jet. Although the model shows an enhancement around $\phi = \pi/2$, it is far from representing the data and the particle densities arising from the two jets cannot be explained by this simple model.

4.6 JETS WITH A PARTICLE WITH LARGE TRANSVERSE MOMENTUM

After the expected four-jet structure in deep inelastic hadron hadron collisions had been established by different types of experiments (DEL77,AKE82,ARN83,BRE84g), a detailed analysis of the structure, charge and flavour correlations should yield more information about the parton interactions. The next sections will mainly describe features of the trigger jet and show that valuable information about the original partons can be extracted from the structure of the trigger jet. This was done in several publications of this group (see e.g. BRE84g). To get a consistent picture about the underlying parton subprocesses it is necessary to study the other jets as well. A detailed study of the away jet properties was the main aim of this analysis and will be presented in chapter 5.

4.6.1 Inclusive cross sections

The p_T dependence of the inclusive cross section for different flavours and charges of the large transverse momentum particle is an important source of information on the parton-parton scattering amplitude. In this experiment the inclusive cross section was measured for identified hadrons at production angles around $\Theta^{tri} \approx 10°, 20°$ and $45°$. The pions were identified by Cherenkov counters. The data were corrected for geometrical acceptance, nuclear absorption in the detector elements, track reconstruction inefficiencies and momentum smearing (DRI82a,PAN82,SPA82). The invariant cross section for inclusive π^+ and π^- production as a function of transverse momentum for a centre-of-mass energy of $\sqrt{s}$ = 62 GeV and for a production angle of $\Theta^{tri} \approx 45°$ is shown in Fig.4.17.

It can be seen that the cross section for positive pions is larger and decreases less steeply than for negative ones. This is an expected behaviour. At larger values of p_T pions dominantly originate from a quark and gluons as the original parton are less probable.

From most fragmentation models (e.g.FEY78) and from e^+e^- annihilation experiments (BRA81a,BGR83), as well as from neutrino-nucleon scattering (ALL83), it follows, that the scattered parton, if it was a quark, is normally contained as a valence quark in the leading particle. This is illustrated in Fig.4.18 where the ratio of the cross sections $\sigma(\pi^+)/\sigma(\pi^-)$ is plotted as a func-

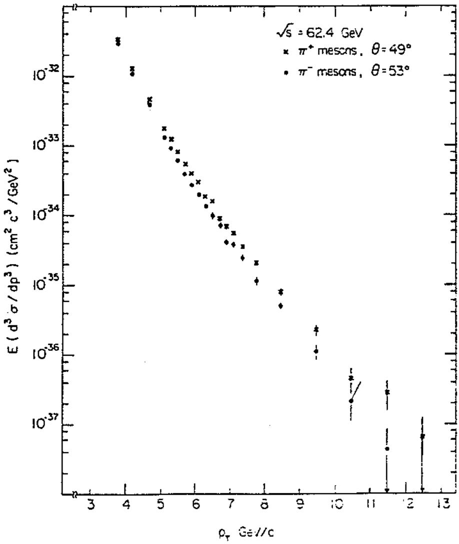

Fig.4.17: Invariant cross section as a function of p_T for positive and negative pions at $\Theta^{tri} \approx 45^o$.

tion of p_T. One expects a ratio around two for large values of p_T corresponding to the ratio of positive and negative valence quarks inside the proton.

The experimental results reflect this qualitative expectation almost perfectly.

4.6.2 Particle ratios

The high-p_T particle, as a leading particle in the jet, is expected to reflect the quantum numbers of the scattered parton. It is therefore of great interest to study the relative yield of particle flavours produced at large transverse momentum. The ratio of π^+/π^- trigger particles, as presented in Fig.4.18 and discussed in the previous section, supports this picture: Large p_T $\pi^+[u\bar{d}]$

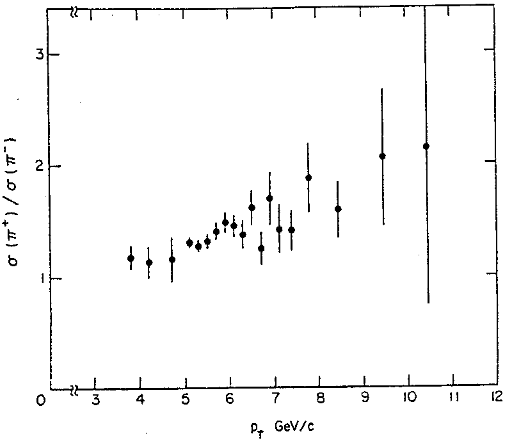

Fig.4.18: The ratio of invariant cross sections $\sigma(\pi^+)/\sigma(\pi^-)$ as a function of p_T for $\Theta^{tri} \approx 45°$.

would preferentially come from a scattered u-quark and $\pi^-[d\bar{u}]$ originate from a scattered d-quark in the region of large Bjorken x where quark scattering is dominant. The ratio π^+/π^- then reflects the valence quark contents of the protons. Since both, $\pi^+[u\bar{d}]$ and $K^+[u\bar{s}]$ contain u-quarks, K^+ triggers should also be leading fragments in u-quark jets. The ratios K^+/π^+ and K^-/π^- are expected to a different p_T dependence. Both, K^+ and π^+, contain u-quarks as valence quarks and, at high values of p_T, are presumably produced by a scattered u-quark picking up an anti-quark from a ss- or dd-system, respectively. Therefore the ratio K^+/π^+ should be independent of p_T and the absolute value reflects the different probability to create a ss- or dd-system from the vacuum (BRE84c).

A high p_T $K^-[s\bar{u}]$ does not contain any valence quark in common with the proton and could be the leading particle in a gluon jet (BRE84g). Since at large p_T the gluon contribution is decreasing (see section 4.6.1), the ratio K^-/π^- should reflect this fact and should decrease as a function of p_T^{tri}. The ratios K^+/π^+ and K^-/π^- are displayed in Fig.4.19 as a function of $x_T = 2 \cdot p_T/\sqrt{s}$ for two different centre-of-mass energies and polar angles around $\Theta \approx 45°$.

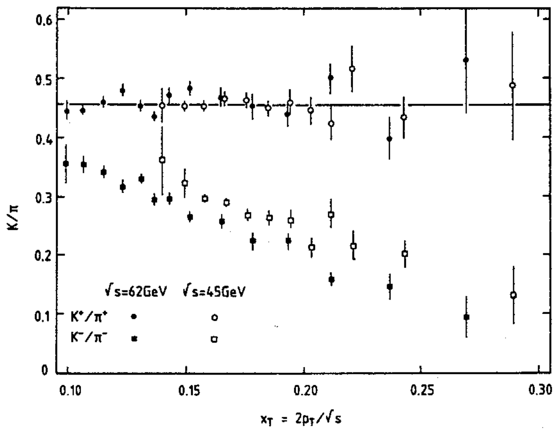

Fig.4.19: Production ratios K^+/π^+ and K^-/π^- for large p_T particles at $\Theta^{tri} \approx 45°$ at c.m.s. energies of $\sqrt{s}$ = 62 GeV and 45 GeV as a function of $x_T = p_T/\sqrt{s}$.

The identification of the trigger particle is performed using Cherenkov counters with a high efficiency. Acceptance effects cancel in the particle ratios. While the ratio K^+/π^+ is constant between x_T = 0.10 and x_T = 0.30, the ratio K^-/π^- decreases with rising x_T in agreement with the expectation.

Another, very interesting problem is the production of baryons at large transverse momentum. With the experimental setup described in 2.2 it was possible to investigate high-p_T baryon production at different polar angles Θ. The particle ratios can yield new information on parton dynamics. The ratio of produced protons (antiprotons) to all positive (negative) particles as a function of the transverse momentum is displayed in Fig.4.20 and 4.21 for three different polar angles, namely at $\Theta^{tri} \approx 10°$, 20° and 45° (BRE84f).
The Θ dependence is presented in Fig.4.22.

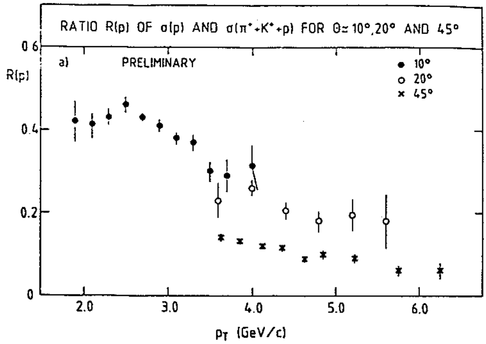

Fig.4.20: σ(proton)/σ(all positive) ratio at large p_T for different polar angles Θ.

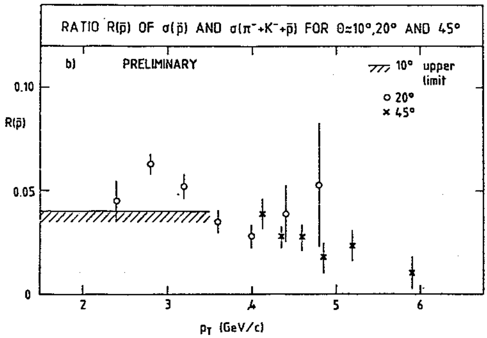

Fig.4.21: σ(antiproton)/σ(all negative) ratio at large p_T for different polar angles Θ.

A very detailed discussion of these results is given in refs. (BRE84f, BRE85a, LOH85). This analysis has shown, that neither the absolute yield nor the p_T and Θ dependence of baryon production can be explained by simple models and a substantial contribution from other processes than those discussed so far have to be taken into account. In particular, it has been shown (BRE85, LOH85) that the scattering of a bound diquark system rather than simple quark or gluon scattering could be an adequate assumption to explain the experimental results (FRE82a, FRE82b, LAR84).

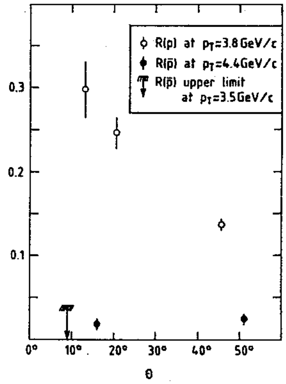

Fig.4.22: Angular dependence of relative baryon production.

4.6.3 Parton flavour identification in high-p_T events

In contrast to jets with a large transverse energy, jets with a large transverse momentum particle appear as the result of a rather exceptional fragmentation process. That is, the production of a leading particle in the jet which carries a large fraction of the total jet energy. This fact allows insights into the nature of the scattered parton which fragments into the trigger jet. This was already mentioned in the previous section and will now be investigated in more detail.

Fractional momentum of the trigger particle

It has been shown earlier (FIS81,BUC82), that the trigger particle carries about 70-80% of the total jet momentum depending on the polar angle and the transverse momentum but independent of the parton flavour (ALO80,ANG82). This effect is known as the "trigger bias" in high-p_T events (ELL74,ELL76,JAC76). The quantity $\langle z^{tri} \rangle$, the mean fraction of the jet momentum carried by the the high-p_T particle, is shown in Fig.4.23 as a function of x_T.

At large values of p_T^{tri} an increasing fraction of the jet momentum is taken by the trigger particle. This dependence has been confirmed by another experiment performed at the CERN ISR (ANG82) triggering on high-p_T π^0.

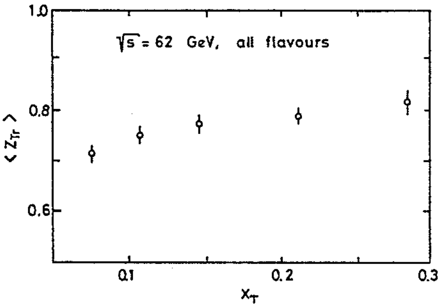

Fig.4.23: Mean fraction of total jet momentum carried by the high p_T particle ("triggerbias") as a function of x_T.

Charge correlations in the trigger jet

As it was argued in the previous section, the quantum numbers of the trigger particle are correlated with the associated particles in the same jet. The density of secondaries in the trigger jet have been determined as a function of z_f:

$$z_f = (p^{sec} \cdot p^{tri}) / |p^{tri}|^2$$

where p^{tri} and p^{sec} are the centre-of-mass momenta of the trigger particle and the secondaries, respectively. The particle density as a function of z_f is shown in Fig.4.24 for different flavours of the trigger particles (BRE84g). Secondaries are displayed with charges equal or opposite to the charge of the high-p_T particle. The data show that the distributions for π^+ and K^+ triggers are similar and suggest that they originate from the same type of partons.

The distributions for π^- and K^- are different. The larger difference between oppositely and equally charged secondaries for K^- triggers imply that K^- triggers preferentially come from a parton which is more neutral than the source of the K^+ triggers. For π^- triggers the difference between the two distributions

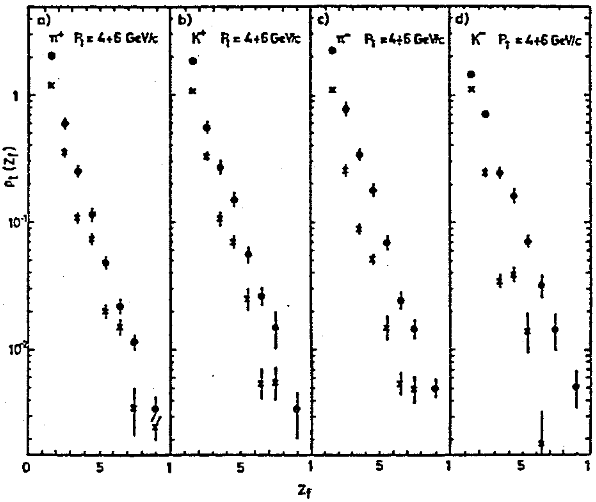

Fig.4.24: Particle density in the trigger jet as a function of z_f for particles with charges equal (crosses) or opposite (dots) to the charge of the trigger.

is smaller than for the K^- but larger than for the π^+/K^+ case. The difference between π^+ and π^- triggers disfavours production of high p_T particles by sea quark scattering since they would result in equal distributions. Dominant production from sea quarks is completely ruled out by the study of strangeness correlations within the trigger jet. It has been shown (RAU82, BRE84g), that the average number of reconstructed, neutral strange particles with $z_f > 0.2$ is more than two times larger for K^+ triggers than for π^+ of π^- triggers. The strangeness is therefore compensated locally within the trigger jet and suggest the picture of producing strange particles at large p_T by creating a ss system in the colour field and not by the fragmentation of a scattered strange sea quark.

Correlations with the spectator jets and resonance production

A scattered valence quark leaves behind a proton remnant which "remembers" the flavour of the scattered parton. The flavour of the trigger particle is therefore correlated with the quantum numbers of particles in the spectator jets. Since the trigger particles are produced at polar angles Θ off 90° in this experiment, in many cases it is possible to associate the two different spectator systems with the trigger jet or the away jet because the spectator jet and the transverse jet coming from then same proton are found in the same hemisphere except for the case of backward scattering. A π^- trigger from a scattered d-quark leaving behind an [uu] system should result in a different spectator structure than a π^+ trigger from a scattered u-quark with a [ud] spectator system. These effects have been studied extensively (DRI79, BRE85g) and the expected correlations have been observed. A very interesting problem is the production of baryons, namely Δ^{++}[uuu] in the spectator jet. The relative production rate should be different for a [u$\bar{d}$] system (π^+ triggers) and a [d$\bar{u}$] system (π^- triggers). Our measurements support this idea very nicely (NAK83, BRE84a, BRE84d). The yield of Δ^{++} is about two times larger for π^- triggers than for π^+ triggers in good qualitative agreement with our expectation.

All these correlations presented here show that in this type of experiment the identification of the leading particle in a jet allows to distinguish between the flavours of the scattered partons fragmenting into the trigger jet. These results are important with respect to the analysis presented in the next chapter where correlations between the two transverse jets are investigated in detail.

5. STRUCTURE OF THE AWAY JET

In the last sections the structure of the trigger jet has been investigated and it has been shown that it is possible to get information about the original parton fragmenting into the trigger jet. It already has been shown in section 4.5.2 that a second transverse jet exists opposite in azimuth to the trigger jet. This second jet is not affected by the trigger bias and therefore, apart from the constraint of four momentum conservation, the recoiling parton has hadronized without the bias of producing a high-p_T particle. This away jet can be used to study parton fragmentation. In the next sections it will be shown, that the inspection of the away jet and its kinematical structure and charge composition together with correlations with the trigger jet can be used to draw conclusions about the underlying scattering process. The parton kinematics and its implication on the geometrical jet structure will be discussed in the first part. In the second part the inclusive distributions are presented and the necessary corrections are described. The differences in the production and fragmentation of quark and gluon jets is then studied using the asymmetry of the away jet and its charge composition. Finally, an attempt is made to compare these inclusive distributions with the results from other types of experiments.

5.1 PARTON KINEMATICS

The direction of the trigger jet is approximately fixed by the trigger condition since the jet direction is almost identical to the trigger direction (BRE84c). This is not true for the away jet if no additional conditions are imposed on it. The two scattered partons are colinear in the parton-parton rest system, but since their fractional beam momenta x_1 and x_2 are in general not equal, the two-parton system is boosted along the direction of the incoming partons. This is illustrated schematically in Fig.5.1.

The collision kinematics of partons with approximately equal fractional parton momenta x_1 and x_2 is shown in Fig.5.1a. The result is a configuration where the two jets are roughly opposite in azimuthal and polar angle in the centre-of-mass system of the two incoming protons. This situation we shall call the "back-to-back" configuration. In Fig.5.1b the partons involved have different values of reduced longitudinal momentum x, such that the Lorentz transformation boosts both transverse partons into the same polar angle hemisphere resulting in the "back-to-antiback" configuration in the proton-proton centre-of-mass system.

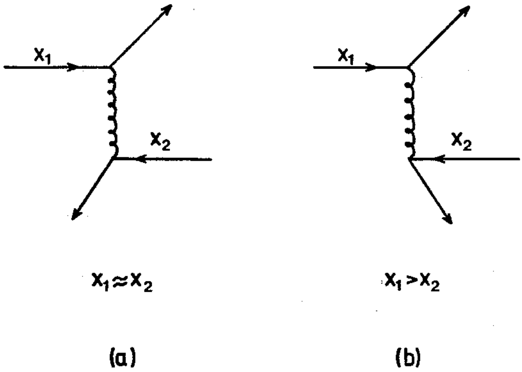

Fig.5.1: Schematic view of parton kinematics.

It was mentioned in section 4.2.1 that the distribution function for gluons is steeper than those for valence quarks. Therefore, partons with large fractional momenta x will mainly be valence quarks and this results in different kinematical configurations for different subprocesses. At large transverse momenta of the trigger particle, events with a back-to-back configuration will essentially come from quark-quark scattering while the interaction between quarks and gluons should result in the back-to-antiback configuration. These correlations will be used later in this chapter to study differences in parton fragmentation.

5.2 PARTICLE DENSITY IN THE AWAY JET

The particle density as a function of rapidity was used in section 4.5.2 to give a first prospect on the jet structure of high-p_T events. Now it will be utilized to study in detail the structure of the away jet. The away jet particles are analyzed within an azimuthal region of $\phi = (\phi^{tri} + 180°) \pm 25°$ to keep the relative contribution from the spectator jets as small as possible.

5.2.1 Jet structure of the away jet

It was shown in section 4.5.2 that the away jet appears as a broad structure opposite in azimuth to the trigger particle while the trigger jet appears as a narrow structure around the direction of the trigger particle. The reason for this difference in structure was explained in the first paragraph of this chapter. In order to show the presence of the away jet we impose an additional condition on the away side similar to the trigger condition. A "pseudotrigger", a leading particle with large transverse momentum on the away side within a limited region in polar angle, is required for each event. The particle density for events which fulfil this condition is shown in Fig.5.2. It shows the same distribution as in Fig.4.20, but with the requirement of a large transverse momentum particle in the away azimuthal region in the rapidity interval of ± 0.4 around the interval indicated by the arrow T'. We require the transverse momenta of the pseudotrigger particles to be larger than $0.3 \cdot p_T^{tri}$. All particles included have transverse momenta above 1 GeV/c and the transverse momenta of the trigger particles are larger than 4 GeV/c at a polar angle around $\Theta^{tri} \approx 45°$.

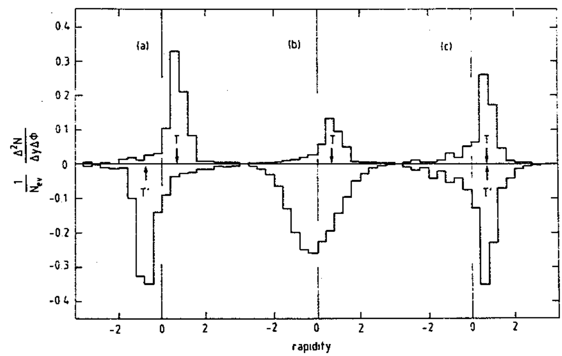

Fig.5.2: Particle density as a function of rapidity y.
A pseudotrigger particle is required in Fig.5.2a (back-to-back) and in Fig.5.2c (back-to-antiback).
All secondaries have p_T > 1 GeV/c.

Neither the trigger nor the pseudotrigger particles are included in the distributions. In Fig.5.2a we demand the pseudotrigger particles to be in the rapidity hemisphere opposite to the trigger particle (back-to-back) while in Fig.5.2c the trigger and pseudotrigger particles are in the same hemisphere (back-to-anti-back). For a comparison, Fig.5.2b shows the distribution without the requirement of a pseudotrigger.

It is clear that the secondaries on the away side follow the direction of the pseudotrigger particles giving the away jet. This is a behaviour which is clearly not expected from simple phase space models. Two transverse jets with approximately the same width are visible.

Another very nice demonstration of the four-jet structure is given in Fig.5.3.

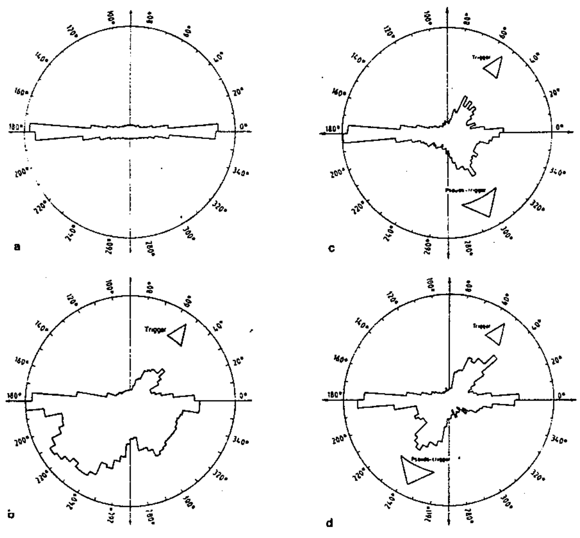

Fig.5.3: Normalized momentum flow projected into the scattering plane as a function of the projected polar angle Θ^{proj}. Trigger particle is at $\Theta^{tri} \approx 45°$ with $p_T > 4$ GeV/c.

It shows the momentum flow of charged particles as a function of the projected polar angle Θ^{proj} in the plane defined by the beam axis and the trigger particle. The flow for normal inelastic events is shown in Fig.5.3a where the flow is concentrated along the beam axis with relatively low transverse momentum. Deep inelastic events with large transverse momentum particles are shown in Fig.5.3b. The trigger particles are at $\Theta^{tri} \approx 45°$ and have transverse momenta larger than 4 GeV/c. It is not included in the momentum flow. The trigger-jet (towards-jet) is clearly visible and a broad structure opposite in azimuth. While the polar angle of the trigger-jet is almost fixed by the trigger condition, the polar angle of the away-jet varies widely. To fix the away-jet within a limited region of the polar angle, a particle with large p_T ($p_T \gtrsim 2$ GeV/c) is required in an angular interval opposite in azimuth to the trigger particle. In Fig.5.3c these pseudotrigger particles are required to be within $\Theta^{proj} \approx 230°$-$260°$ (back-to-antiback) and in Fig.5.3d within $\Theta^{proj} \approx 280°$-$310°$ (back-to-back). The pseudotrigger particles are not included in the distributions. It appears that the particle density follows the pseudo-trigger direction and a distinct four-jet structure is now clearly visible including two longitudinal jets following the beam directions (spectator-jets).

5.2.2 Jet structure for different polar angles of the trigger

An interesting question is the particle density in the away jet for different polar angles of the trigger particle and at fixed values for the trigger transverse momentum. Since the statistics is very low for $\Theta^{tri} \approx 10°$ and $20°$ for trigger transverse momenta above 4.0 GeV/c, a special sample of events has been recorded for comparison with transverse momenta between 1.8 GeV/c and 4.0 GeV/c at $\Theta^{tri} \approx 45°$. The particle density for events with $2.0 \lesssim p_T^{tri} \lesssim 4.0$ GeV/c at three different polar angles is shown in Fig.5.4. All secondaries have $p_T \gtrsim 1.0$ GeV/c. The particle density in the trigger region is plotted upwards, the density in the away region is plotted downwards.

For equal transverse momenta of the trigger jet, neglecting effects originating from the transverse motion of the partons and the different subprocesses, the integrated particle density would be approximately equal if the momentum of the away jet can be approximated by the transverse momentum of the trigger particle. The data show a different trend: the particle density in the away jet is decreasing if the polar angle decreases. This can be qualitatively understood as an effect of the "trigger bias". The fraction of the jet momentum taken by the leading particle is larger for smaller polar angles of the trigger. There-

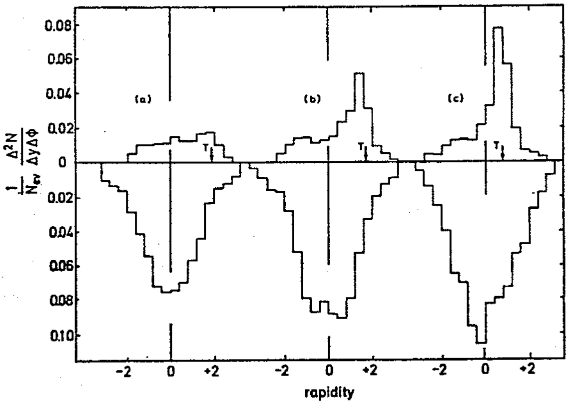

Fig.5.4: Particle density for events with $2.0 \lesssim p_T \lesssim 4.0$ GeV/c at polar angles of 10° (a), 20° (b) and 45° (c).

fore, at fixed values of p_T^{tri}, the total jet momentum is larger for $\Theta^{tri} \approx 45°$, where $\langle z^{tri} \rangle$ is around 0.75, than for $\Theta^{tri} \approx 20°$ or 10° with $\langle z^{tri} \rangle \approx .85$. This effect is even more drastic on the particle density in the trigger jet as it can be seen from Fig.5.4. Compared to the pronounced jet structure for triggers at $\Theta^{tri} \approx 45°$ and 20° the trigger jet is almost invisible for triggers around $\Theta^{tri} \approx 10°$. The energy available for the production of secondaries in the trigger jet varies by more than a factor two when changing from 45° to 10°.

For very forward angles the trigger jet mainly consists of one very fast particle - the trigger particle - with a total momentum of up to 25 GeV/c. The Bjorken x of the scattered parton fragmenting into the trigger jet is increasing when the scattering angle is decreased. This results in the very fast forward trigger particle and has some implications on the studies of the away jet properties. The remaining energy available is different for the two spectator systems associated with the trigger jet and the away jet, resulting in a highly asymmetric particle distribution. Since it is always tedious to separate the spectator system from the away jet, especially for the forward angles with low-p_T fragments, the away jet distributions can be highly distorted for those events with a forward trigger particle. Therefore, the data with triggers at $\Theta^{tri} \approx 10°$ were not used for the following studies.

5.3 HADRON SPECTRA IN THE AWAY JET

For a detailed analysis of the away jet structure, it is necessary to study the momentum spectra of the away jet fragments. The longitudinal structure of hadron jets in e^+e^- collisions is normally studied using the variable z:

$$z = E_H/E_{max}$$

where E_H is the hadron energy and E_{max} is the total jet energy which is identical to the energy of the incoming electrons or positrons in normal two jet events (WUS84).

Unfortunately the total jet energy is not known for high-p_T proton-proton collisions because the collision energy of the scattered partons is not fixed. In order to study the trigger jet, the variable z_f has been used which approximates the jet momentum by the momentum of the trigger particle. Because the trigger particle is a leading particle in the trigger jet, this is a good approximation for the momentum and direction of this jet (section 4.7.1). The situation is more complicated for the away jet recoiling against the trigger jet. It normally does not contain a leading particle, therefore the away jet direction and its momentum is unknown. Neglecting transverse momenta of the incoming partons, the transverse momentum of the trigger jet is balanced by the away jet and to study the properties of the away jet fragmentation, the variable x_E is used. It measures the fraction of the trigger transverse momentum balanced by a particle in the away jet. It is defined as:

$$x_E = p_T/p_T^{tri}$$

where p_T is the transverse momentum of a secondary particle in the away jet. Since x_E is correlated with the correct fragmentation variable:

$$z = p/p_{parton} \quad (p_{parton} = \text{total parton energy})$$

it is a good approximation to study the fragmentation properties of the away jet. Note that the values for x_E might exceed one with this definition. One feature of this variable should be mentioned here. Since the spectra are influenced by the "trigger bias", the momentum fraction taken by the leading particle in the trigger jet, comparisons between different spectra should be performed at equal transverse momenta of the trigger particle because of the p_T dependence of the trigger bias. Trigger jets originating from partons with different fragmentation functions, e.g. gluons and quarks, influence the slope of the away jet x_E-distribution differently and should be analyzed separately.

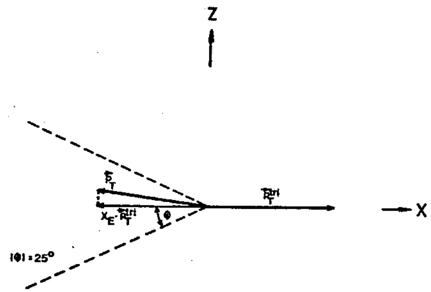

Fig.5.5: Definition of x_E and azimuthal region for the away jet distributions.

It is therefore important to have information about the origin of the trigger jet in order to distinguish between dynamical and purely kinematical effects.

After the description of the corrections, which have to be applied to obtain the true x_E-distributions, the analysis of charge composition and asymmetry of the away jet will be used to study the structure of the recoiling jet and the underlying scattering process in the framework of the quark parton model.

5.3.1 Corrections

Several effects cause the measured x_E-distributions to be different from the true ones. The geometrical acceptance of the detector and the efficiency of the reconstruction program have to be taken into account. The contribution from the longitudinal spectator jets at low values of x_E have to be subtracted. A loss arises from the geometrical definition of the away jet for the analysis. For the x_E-distributions only particles are considered within a finite wedge of the azimuthal angle (Fig.5.5). Only particles within $\phi = 180° \pm 25°$ with respect to the trigger particle are used. For low values of x_E, the away jet is not completely included within this wedge and the distributions have to be corrected for these losses.

Acceptance correction

The geometry of the detector and the shape of the magnetic field of the Split-Field Magnet causes strong variation of the acceptance in some regions of the phase space. Particles with low transverse momenta in the forward direction have a small acceptance since they leave the beampipe too late and escape detection. In the central region of the detector the magnetic field is weak, therefore the momentum resolution is relatively poor and varies strongly with the azimuthal angle.

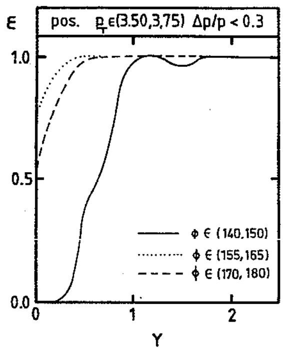

Fig.5.6: Acceptance for positive particles at different angles.

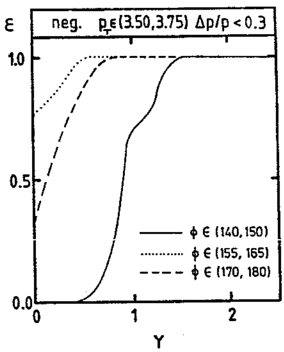

Fig.5.7: Acceptance for negative particles at different angles.

For particles with larger values of p_T (p_T>1.0 GeV/c) in the region around $\Phi\approx90°$ the momentum resolution is usually worse than $\Delta p/p$ > 30-50% for both charges. To avoid the use of tracks with poorly measured momentum or a wrongly determined charge, one has to require a sufficient accuracy for the momentum determination. A relative accuracy of $\Delta p/p \lesssim 0.30$ was used for all distributions presented in this analysis. For this accuracy the acceptance is good for azimuthal angles around $\phi\approx0°$ and $\phi\approx180°$ but it decreases to zero for rapidities lower than 1 and azimuthal angles outside a wedge of ±25 with respect to ϕ=0° and ϕ=180°. As an illustration, the acceptance as a function of rapidity is shown in Fig.5.6 and Fig.5.7 for positive and negative particles produced around an azimuthal angle of ϕ=180°. Since we cannot correct in regions where the acceptance is zero, the analysis is performed for particles within this azimuthal interval of ±25° only. The effect of the acceptance correction is demonstrated in Fig.5.8 where the observed and uncorrected x_E-distribution for positive secondaries with a π^+ trigger particle is compared to the acceptance corrected one.

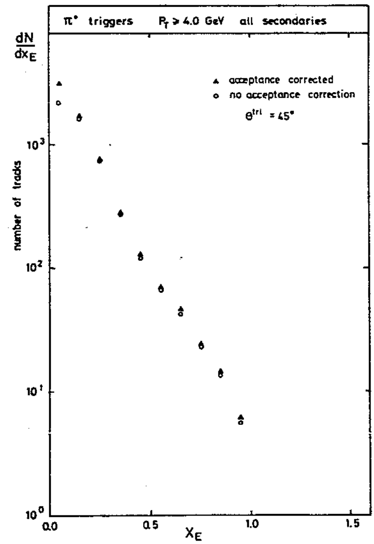

Fig.5.8: x_E distribution for π^+ triggers at 45° with and without acceptance correction.

It shows that the correction is relatively small over the x_E range investigated and does not change the original distribution too much except at very low values of x_E where fragments from the spectator jets are dominating. The overall average acceptance correction amounts to $\langle 1/\varepsilon \rangle \approx 1.16$. The very small correction factor for particles with x_E around 1.0 needs some explanation. The calculated acceptance is a convolution of the track finding and track detection efficiency and the momentum shift due to the finite momentum resolution. A detailed study has shown that both effects amount to about 20-30% around x_E = 1.0 for both charges. Since these two effects shift the distribution in opposite directions almost cancel resulting in an acceptance close to one and wrongly pretend a very high track reconstruction efficiency in this region.

Subtraction of spectator background

The x_E-distribution in Fig.5.8 contains the contribution from both, the away jet and the spectator jets. To obtain the true distribution for the away jet, the spectator contribution has to be subtracted. Since the spectator distributions are not directly measurable And we do not trust in model calculations, we have used an experimental approach. The fragmentation of the spectator system is believed to be similar to normal inelastic collisions, so called "minimum bias" events. A trigger particle is simulated according to measured distributions and combined with a normal inelastic event (Fig.5.9).

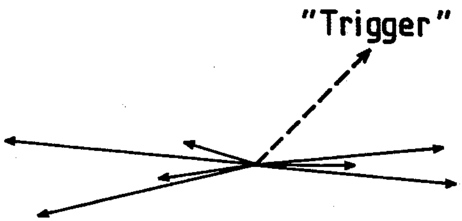

Fig.5.9: Schematic sketch of a normal inelastic event combined with a simulated high-p_T trigger particle.

The x_E-distributions are then determined as it is done for high-p_T events. This has the advantage that the spectator contribution can be estimated in the same detector region where the away jet is studied. The spectator contribution determined with such method is shown in Fig.5.10 for both, the back-to-back and the back-to-antiback configurations, together with a distribution for events with a high-p_T π^+ trigger.

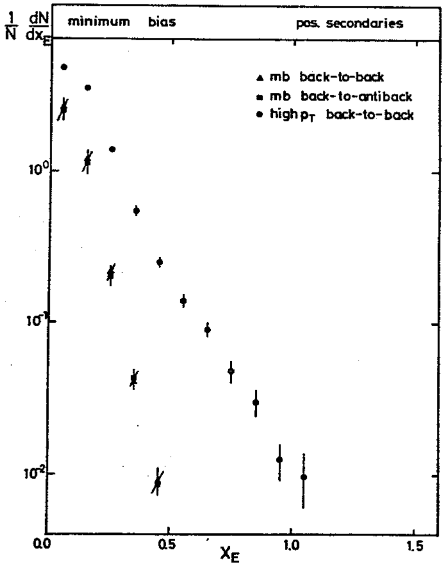

Fig.5.10: Spectator contribution estimated from inelastic events compared with high-p_T x_E-distribution.

It shows that the spectator systems only contribute at small values of x_E, and the contribution drops below 1% above $x_E \approx 0.5$.

Azimuthal acceptance

To keep the relative contribution from spectator fragments as small as possible and to guarantee a large and smooth acceptance over the region investigated, the away jet is analyzed in a limited azimuthal angle (Fig.5.6). The transverse momenta with respect to the parton direction arising from the fragmentation are limited and the fragments will be approximately confined within this wedge. The inspection of Fig.4.16 suggests that the away jet extends to azimuthal angles beyond these limits, especially for secondary particles with low transverse momentum. It is therefore necessary to correct for these p_T dependent losses. Unfortunately it is not possible to correct in a model independent way since the azimuthal distribution is crucial to the correction factors. A version of the LUND model for high-p_T events (BEN85) has been used where the scattered partons fragment independently with the possibility to associate every individual particle to its ancestor. This allows a determination of the percentage of away jet particles included within the region of the limited azimuthal angle of $\Delta\phi \pm 25°$. This azimuthal acceptance is presented in Fig.5.11 as a function of x_E for trigger particles around $\Theta^{tri} \approx 45°$ with $p_T^{tri} \geq 4.0$ GeV/c and in Fig.5.12 for trigger particles around $\Theta^{tri} \approx 20°$ with $p_T^{tri} \geq 2.0$ GeV/c.

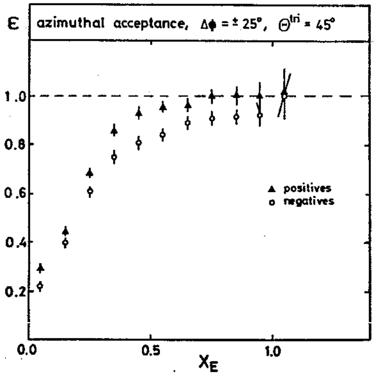

Fig.5.11: Azimuthal acceptance for $\Theta^{tri} \approx 45°$.

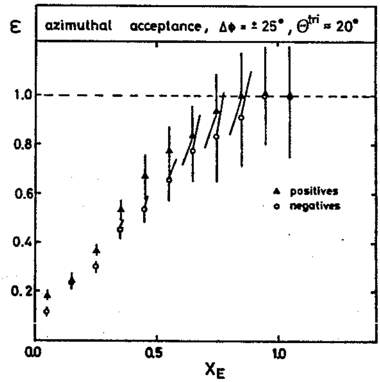

Fig.5.12: Azimuthal acceptance for $\Theta^{tri} \approx 20°$.

Positive and negative secondaries are plotted separately. It shows that, at low values of x_E, a large fraction of the away jet particles is not included within the azimuthal wedge whilst for values of x_E above 0.5 the away jet is entirely contained within the defined region. The x_E-distributions presented in this analysis are corrected for these losses.

5.3.2 Experimental results for $\Theta^{tri} \approx 45°$

In this section, the inclusive spectra of hadrons in the away jet are presented as a function of x_E for high-p_T triggers at $\Theta^{tri} \approx 45°$ and $\Theta^{tri} \approx 20°$. First, the x_E-distributions $1/N_{ev} \cdot dN/dx_E$ are shown for positive and negative secondaries for different flavours of the trigger particles. Secondly, equivalent distributions are presented for different configurations of the transverse jets, i.e. the back-to-back and back-to-antiback configuration. The naive quark parton model predicts differences between these two configurations. These differences are verified and compared to the predictions from the LUND program using independent fragmentation. The use of a fragmentation model where the partons fragment independently makes it possible to study the secondaries of the away parton separately and compare it to the measured distributions.

Distributions for positive and negative secondaries

The distributions $1/N \cdot dN/dx_E$ for positive and negative particles are shown in Fig.5.13 for events with π^+ and π^- triggers summed over all particles in the away region defined in Fig.5.6 and corrected as described in the previous section.

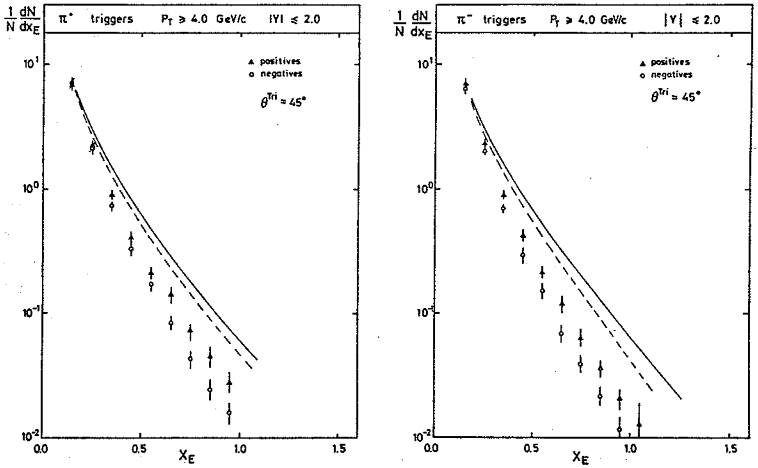

Fig.5.13: Inclusive x_E-distributions for π^+- and π^--triggers. Lines are prediction from the LUND program (BEN85) for positive (full lines) and negative (dashed lines) secondaries.

It was shown in Fig.4.20 for trigger particles at $\Theta^{tri} \approx 45°$ and in Figs.4.22 and 4.23 for the forward triggers that the away jet extends to rapidities of about 2.0. To minimize the relative contributions from the spectators and the uncertainties in their subtraction, the rapidity range of the away jet distributions are limited to absolute values lower than two. As can be seen from Fig.5.13, these single particle inclusive spectra for charged hadrons decrease strongly as a function of x_E and they are different for positive and negative particles. At large Bjorken x of the scattered away parton, the away jet particles are predominantly fragments of a valence quark. Provided that all away particles are due to fragmented gluons, no difference is expected between positive and negative particle spectra. This is clearly ruled out by the data. Secondaries in the away jet with large values of x_E, for instance $x_E \geq 0.5$, are leading particles in the away jet and are expected to reflect the quantum numbers of the scattered partons as demonstrated for the trigger jet. At large values of x_E, an excess of positive particles is therefore expected from the quark content of the proton. This is discussed quantitatively in a later section using charge ratios of secondaries in the away jet.

The inserted lines are the predictions from the LUND program for high-p_T events (BEN85) using independent fragmentation. Full lines correspond to positive particles and dashed lines to negative ones. The particle spectra are overestimated by the model. The discrepancies between the data and the model could be eliminated by the introduction of unnatural large values of $\langle k_T \rangle$. It is also possible that the insertion of initial and final state bremsstrahlung could improve the model predictions. The radiation of gluons before and after the hard scattering process would result in a steeper slope of the x_E-distributions because the available energy is shared between the gluon and the original parton. The away side region would be populated by fragments from the scattered parton plus one or more low energetic jets from radiated gluons (Fig.5.14) appearing as a multijet event. Qualitatively, a different slope for quark and gluon jets can be understood and is even expected in this picture. Radiative gluons couple stronger to scattered gluons than to scattered quarks because they are colour octets and quarks are colour triplets. Therefore gluon bremsstrahlung occurs more frequently for gluon jets than for quark jets leading to a softer particle spectrum for gluon jets.

The distributions for positive and negative kaons are displayed in Fig.5.15 together with the predictions from the LUND program.

It should be noted that the event samples with positive and negative kaon triggers are contaminated by baryons. The sample with K^+ triggers contains approximately 20-25% protons at a transverse momentum of 4 GeV/c and the K^-

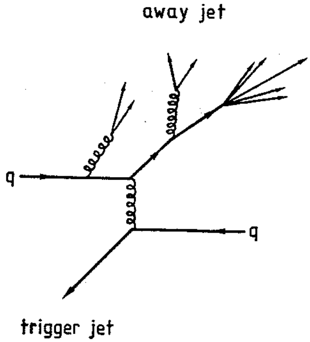

Fig.5.14: Initial and final state gluon bremsstrahlung leading to multijet events.

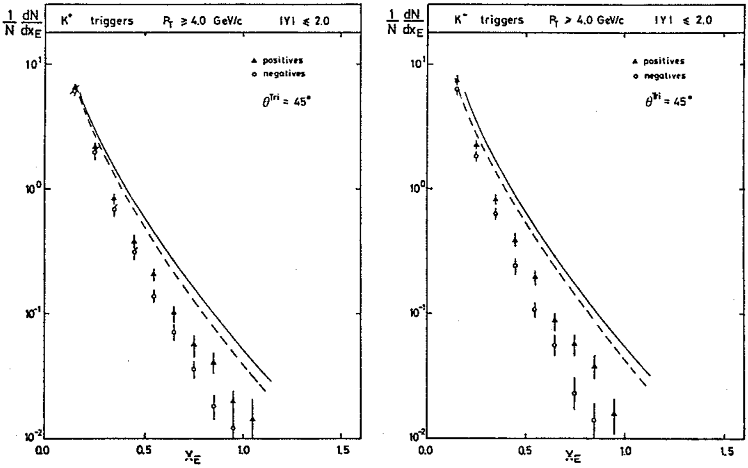

Fig.5.15: Inclusive x_E-distributions for K^+- and K^--triggers. Lines are prediction from the LUND program (BEN85) for positive (full lines) and negative (dashed lines) secondaries.

triggers are contaminated with about 5% antiprotons. The observations which can be made are very similar to those for pions. Actually, one expects no difference between K^+ and π^+ triggers since both are believed to be produced by an identical scattering process (BRE84g). A difference should arise from different subprocesses which result in distinct configurations of the two jets. It is therefore necessary to study the distributions separately for the back-to-back and the back-to-antiback arrangement.

Distributions for different kinematical configurations

It was argued in section 5.1 that the hard collisions of partons with strongly different momenta result in a back-to-antiback configuration of the two transverse jets: the trigger jet and the away jet are found in the same rapidity hemisphere. The dominant scattering process leading to the back-to-back configuration at large transverse momenta should be the scattering of two valence quarks while the back-to-antiback region would be mainly populated by fragments of a quark-gluon scattering process. The x_E-distributions in the two different regions should exhibit this fact and show differences in the distributions as well as in the charge structure of the away jet. The distributions for positive and negative secondaries for the back-to-back and back-to-antiback configuration are shown in Fig.5.16 for events with a π^+ trigger at $\Theta \approx 45°$.

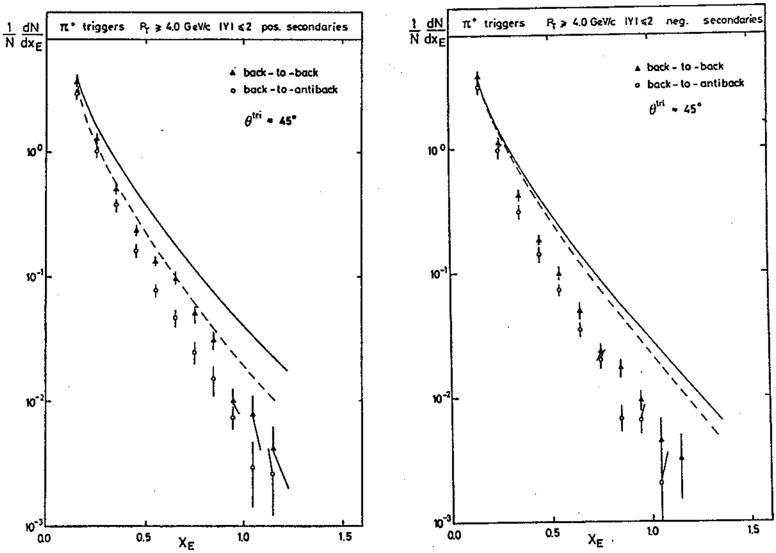

Fig.5.16: Inclusive x_E-distributions for π^+-triggers for the back-to-back and back-to-antiback regions. Lines are predictions from the LUND program (BEN85) for the back-to-back (full lines) and the back-to-antiback (dashed lines) regions.

In both cases the transverse momenta of the triggering particles are larger than 4.0 GeV/c. A clear trend is visible for both charges of the secondaries: the distributions of particles in the back-to-back region are higher than those for particles in the back-to-antiback region and the ratio between those distributions is increasing with increasing x_E. Two effects can be the origin for a larger particle density in the back-to-back hemisphere and can produce this asymmetry of the away jet. First, four momentum conservation could be a trivial explanation for this effect. Secondly, it is possible that for events with a π^+ trigger particle the back-to-back configuration is preferred by the parton kinematics leading to a parton with a softer fragmentation function in the back-to-antiback region as indicated by the steeper slope of the distribution. The same behaviour should be found for events with K^+ triggers and this is demonstrated in Fig.5.17 where the equivalent distributions are plotted.

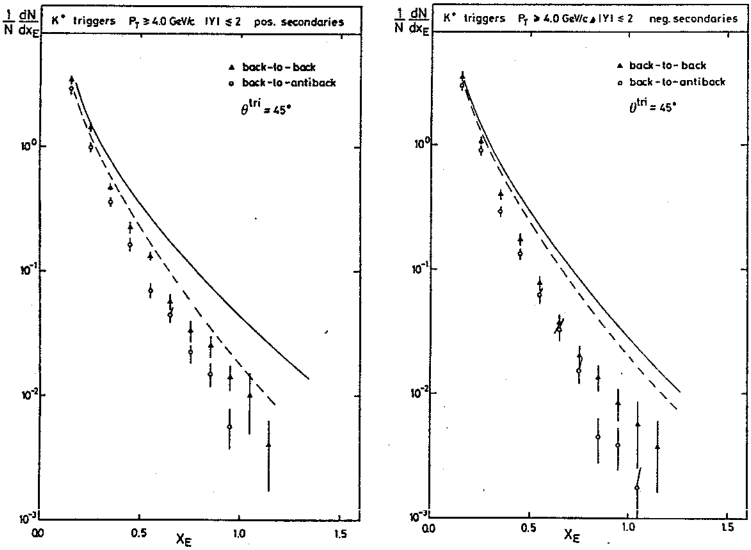

Fig.5.17: Inclusive x_E-distributions for K^+-triggers for the back-to-back and back-to-antiback regions. Lines are predictions from the LUND program (BEN85) for the back-to-back (full lines) and the back-to-antiback (dashed lines) regions.

If the asymmetry of the away jet is due to simple momentum conservation one would expect the same effect for events where the trigger particles originated from gluons. It is therefore interesting to look at the distributions for events with a K^- trigger particle which is most probably a leading particle in a gluon jet. The distributions for positive and negative particles in the back-to-back and the back-to-antiback regions are shown in Fig.5.18 for K^- triggers at $\Theta \approx 45^0$ with $p_T^{tri} \geq 4.0$ GeV/c.

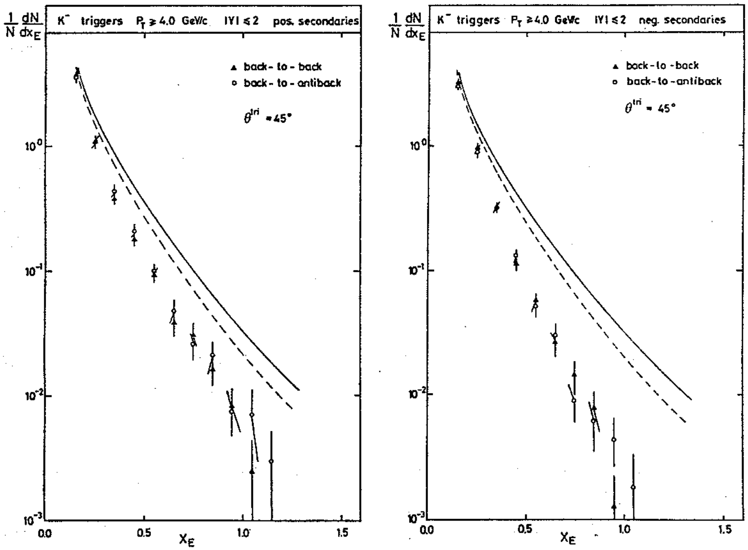

Fig.5.18: Inclusive x_E-distributions for K^--triggers for the back-to-back and back-to-antiback regions. Lines are predictions from the LUND program (BEN85) for the back-to-back (full lines) and the back-to-antiback (dashed lines) regions.

While the kinematical situation is rather distinct for the case of a trigger jet originating from a quark, events are different when the ancestor of the trigger particle is a gluon. Now we have to deal with the two subprocesses gluon-quark and gluon-gluon scattering. Jets with a K^+ or π^+ trigger favour quarks with large values of Bjorken x. This is not the case for gluon jets and the kinematical configuration can be complicated. Both away regions are populated by gluon jets as well as quark jets. We therefore do not expect such a clear and distinct difference between the back-to-back and the back-to-antiback distributions. This can be seen in Fig.5.19: no significant difference can be observed either for the positive or for the negative secondaries in case of K^- triggers and this indicates a smaller contribution of quark jets in the back-to-back configuration. This difference from the data with K^+ or π^+ triggers is a strong indication that this asymmetry is not only due to simple momentum conservation. The away jet asymmetry is discussed quantitatively in the next section.

To provide more confidence that this asymmetry is not due to purely kinematical effects or quantum number conservation constraints, the distributions for positive and negative secondaries in the back-to-back and the back-to-antiback regions are shown in Fig.5.19 for events with a π^- trigger particle. Possible effects which could come from the different charge of the trigger particle in the comparison between π^+ and K^- triggers would not show up.

In our hard scattering picture, the π^- triggers are believed to be mainly fragments of a valence d-quark (BRE84g) and are expected show a similar behaviour as events with π^+ triggers.

This is qualitatively verified by the distributions displayed in Fig.5.19 and proves that the observed away jet asymmetry is not due to purely kinematical effects since they would produce similar effects for events with K^- and π^- triggers.

5.3.3 Experimental results for $\Theta^{tri} \approx 20°$

The distributions $1/N \cdot dN/dx_E$ for positive and negative secondaries in events with positive and negative trigger particles produced at a polar angle around 20° are plotted in Fig.5.20. The lines represent the predictions from the LUND Monte-Carlo with independent fragmentation of the partons.

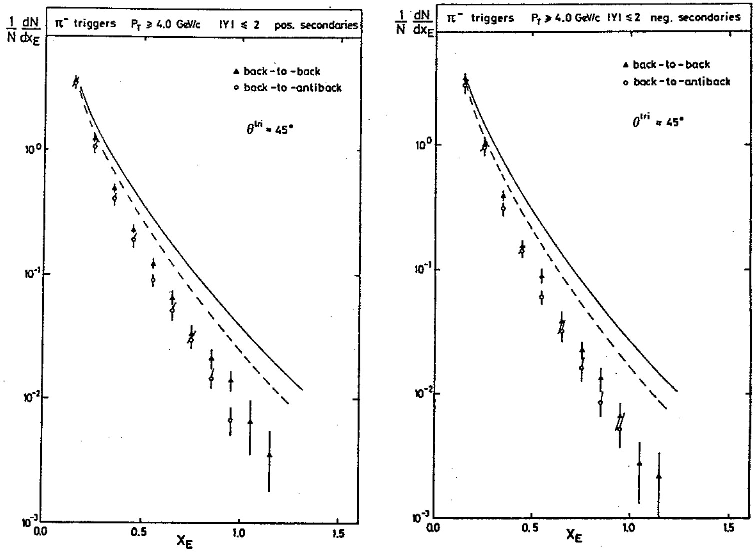

Fig.5.19: Inclusive x_E-distributions for π^--triggers for the back-to-back and back-to-antiback regions. Lines are predictions from the LUND program (BEN85) for the back-to-back (full lines) and the back-to-antiback (dashed lines) regions.

One striking difference can be observed when compared to the distributions with triggers at 45°. The difference between the distributions for negative and positive particles is less pronounced and indicate a larger contribution from gluons fragmenting into the away jet. This is supported by Fig.5.21 where the distributions for positive secondaries in events with a positive trigger particles are plotted separately for the back-to-back and the back-to-antiback region.

The difference between these configurations is not so distinct as observed for triggers at 45°, indicating a strong gluon component in the back-to-back region. For comparison the Fig.5.21a is combined with the distributions for positive secondaries in the back-to-back and the back-to-antiback regions for triggers around 45° with transverse momenta above 2 GeV/c.

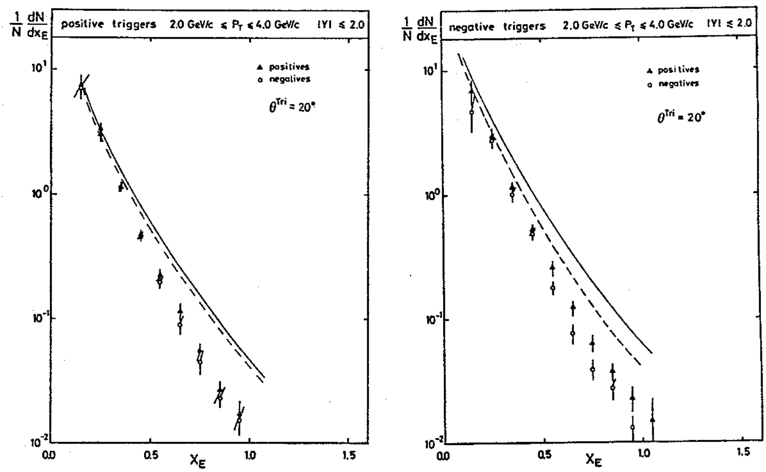

Fig.5.20: Inclusive x_E-distributions for triggers at $\Theta^{tri} \approx 20°$. Lines are predictions from the LUND program (BEN85) for positive (full lines) and negative (dashed lines) secondaries.

The slopes of both distributions for triggers at 20° are closer to those in the back-to-antiback regions for triggers at 45° although an absolute comparison is difficult since the values of the trigger bias is different for the two data samples and pushes the distributions for triggers at 20° towards a steeper slope. Nevertheless, this result should be treated as a hint and a better comparison can be performed in terms of the charge structure and will be made in a later section.

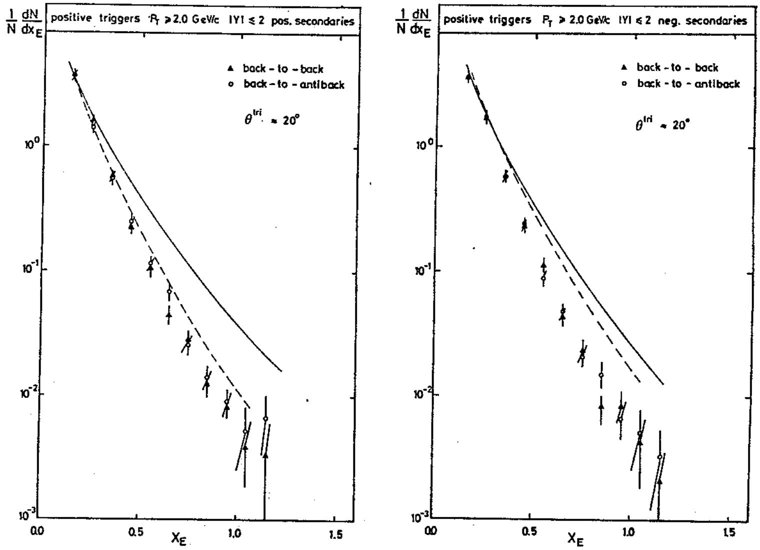

Fig.5.21: Inclusive x_E-distributions for positive triggers for the back-to-back and back-to-antiback regions. Lines are predictions from the LUND program (BEN85) for the back-to-back (full lines) and back-to-antiback (dashed lines) regions.

5.3.4 Away jet asymmetry

To provide a quantitative test of the away jet asymmetry, one can define a variable to measure the relative particle densities back-to-back and back-to-antiback. In this analysis the variable R is used, defined as:

$$R = \frac{\text{particle density back-to-back}}{\text{particle density back-to-antiback}}$$

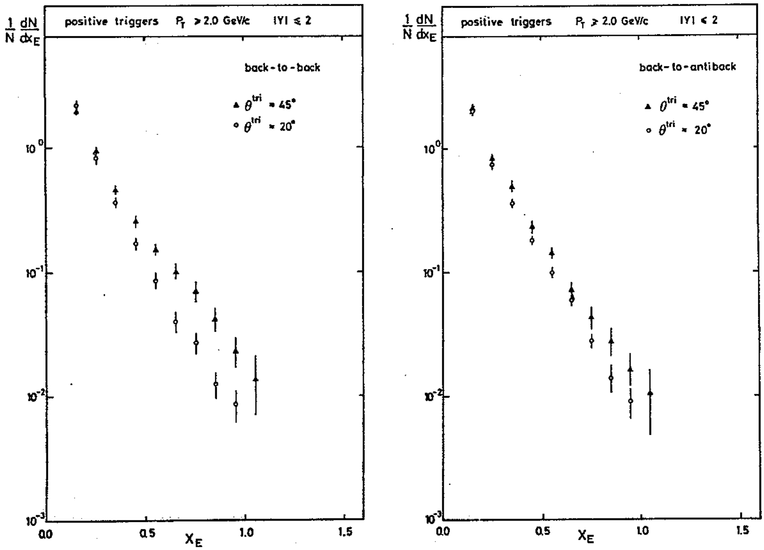

Fig.5.22: Inclusive x_E-distributions for positive triggers in the back-to-back and back-to-antiback configurations for triggers at 20° and 45°. Positive secondaries are shown only.

which measures the shift from a roughly symmetric distribution ($R \approx 1$) to a colinear distribution ($R > 1$) as a function of the variable x_E.

The global rapidity distributions presented in section 4.5.2 showed already the tendency of a shift from a symmetric distribution around $y=0$ to a asymmetric distribution with a back-to-back configuration of the two transverse jets when the trigger transverse momentum was increased (Fig.4.20). This is now illustrated in a different way in Fig.5.23 where the asymmetry R is shown for three intervals of the trigger transverse momentum for events with a π^+ trigger particle at $\Theta^{tri} \approx 45°$.

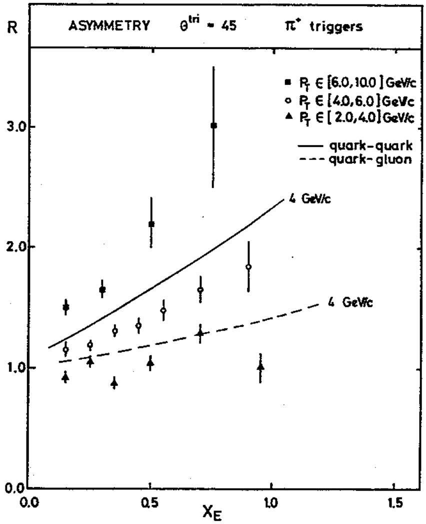

Fig.5.23: Asymmetry for three intervals of p_T^{tri} for π^+ triggers at $\Theta^{tri} \approx 45°$.
Lines are predictions from the LUND Monte-Carlo program for pure quark-quark (full line) and quark-gluon (dashed line) scattering for $p_T > 4.0$ GeV/c.

It is clearly visible that the asymmetry R is strongly increasing with p_T^{tri} and rising with x_E for a given interval in p_T^{tri}. This trend may be due to pure momentum conservation which would shift the away jet into a colinear configuration if the transverse momentum of the trigger particle increases. However, this shift would also occur if the relative importance of the various subprocesses changes with p_T^{tri}. A relative increase of quark-quark scattering with increasing transverse momentum of the trigger particle would also result in a shift of the away jet and the towards jet into a colinear configuration since it is favoured by the parton kinematics. For an illustration of this behaviour, the results of a QCD model calculation for pure quark-quark and quark-gluon scattering are plotted separately in Fig.5.23 for a transverse momentum of the trigger particle above 4.0 GeV/c . It shows that the experimental data lie between the extremes of pure quark-quark and pure quark-gluon scattering. A similar behaviour can be observed for triggers at $\Theta^{tri} \approx 20°$ as presented in Fig.5.24 for three intervals of p_T^{tri}.

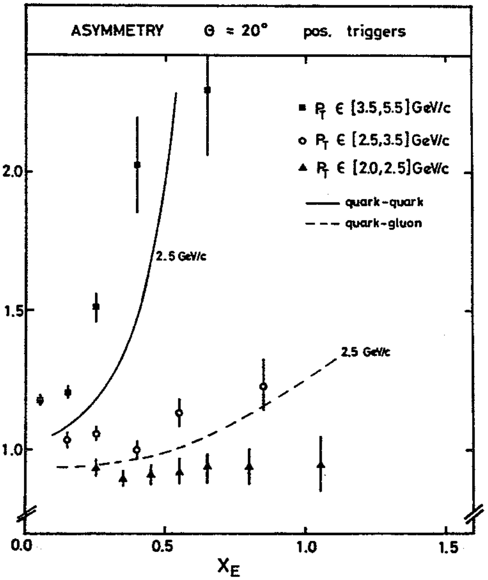

Fig.5.24: Asymmetry for three intervals of p_T^{tri} for positive triggers at $\Theta^{tri} \approx 20°$. Lines are predictions from the LUND Monte-Carlo program for pure quark-quark (full line) and quark-gluon (dashed line) scattering for $p_T > 2.0$ GeV/c.

Although a quantitative comparison between the two data samples at $\Theta^{tri} \approx 45°$ and 20° is very difficult, the tendency to shift to a colinear configuration for large p_T^{tri} is clear for both angles.

The argument that momentum conservation is not the main process leading to this asymmetry can now be studied quantitatively.

In Fig.5.25 the asymmetry as a function of x_E is given for different flavours of the trigger particles produced at $\Theta^{tri} \approx 45°$ with a transverse momentum between 4.0 GeV/c and 6.0 GeV/c. The behaviour is different for the various trigger flavours. If momentum conservation would play the most important role for the away jet asymmetry, no differences are expected between the four data samples. The data shown in Fig.5.25 seem to support the picture that π^+ and K^+ triggers most probably originate from a valence u-quark while K^- triggers come from a fragmenting gluon. For π^+ and K^+ triggers the asymmetry R is steeply rising as a function of x_E, while for K^- triggers it is consistent with a constant around unity, i.e. no asymmetry, as expected from pure quark-gluon scattering.

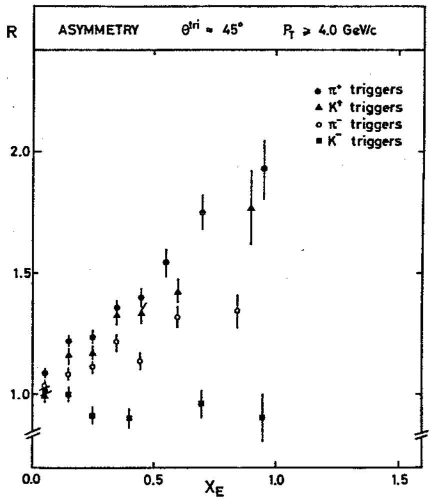

Fig.5.25: Asymmetry for different flavours of the trigger particle for 4.0 GeV/c $\lesssim p_T^{tri} \lesssim$ 6.0 GeV/c.

The asymmetries for π^+ and K^+ triggers are equal within the experimental errors over the whole x_E range investigated as expected. This also gives experimental evidence that away jet production in high-p_T events is not a simple consequence of conservation of transverse momentum and that K^- trigger particles are produced by a production mechanism different from that for π^+, π^- and K^+ mesons. If one assumes that quark-gluon scattering is the dominant process in the p_T^{tri} range investigated, K^- triggers would enrich quark jets on the away side (GLU81) while π^+, π^- and K^+ triggers would enrich gluons jets.

Since quarks carry electromagnetic charge and gluons are neutral, this should result in a different charge structure of the away jet. This charge structure of the away jet will be studied in the next section.

5.3.5 Away side charge ratio

The shift of the particle density to a back-to-back configuration with growing transverse momentum of the trigger particle was interpreted as an increase of the relative importance of quark-quark scattering in events with a particle with large transverse momentum. Since the proton has a larger relative abundance of positive quarks than negatives, jets from a proton valence quark should, on the average, have a higher density of positive particles than negatives. To formulate this idea quantitatively, the ratio $R^{+/-}$ is used, defined as:

$$R^{+/-} = \frac{\text{density of positive particles}}{\text{density of negative particles}}$$

and is studied as a function of x_E and p_T^{tri}.

Charge ratio as a function of p_T^{tri}

One can resume the study of the p_T^{tri} dependence performed for the away side asymmetry in the last section.

In Fig.5.26 the charge ratio in the back-to-back region is plotted for π^+ triggers at $\Theta^{tri} \approx 45°$ for three different intervals of p_T^{tri} as a function of x_E. The back-to-back region was chosen because fragments from valence quarks are expected to be found there and the interpretation of the results is straightforward.

The charge ratio is increasing with the transverse momentum of the trigger particle indicating an increasing importance of valence quark scattering. A more appropriate representation is used in Fig.5.27. For two intervals of x_E (0.2-0.3 and 0.6-0.7) the charge ratio is plotted as a function of p_T^{tri}.

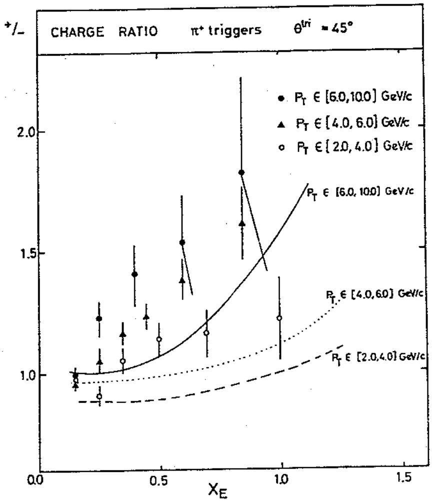

Fig.5.26: Charge ratios $R^{+/-}$ for different intervals of p_T^{tri} for triggers at 45°.

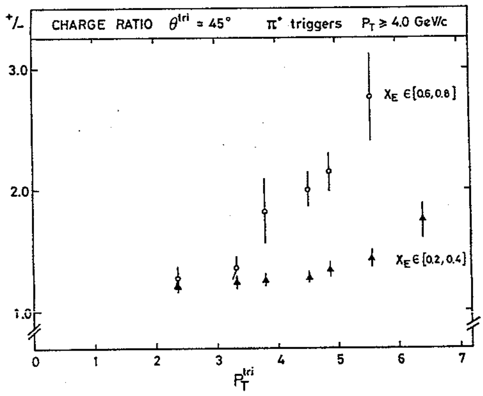

Fig.5.27: Charge ratios $R^{+/-}$ for two intervals of x_E as a function of trigger transverse momentum.

Two effects are clearly visible: the charge ratio $R^{+/-}$ is increasing with p_T^{tri} for both intervals as already expected from the inspection of Fig.5.26. The second effect cannot be observed easily in Fig.5.26: the increase of the charge ratio is much more distinct and larger for higher values of x_E. Particles with x_E above 0.6 are leading particles in the away jet and most probably contain the original parton. Therefore this strong increase of the charge ratio is expected.

Charge ratio for different trigger particles

The different magnitudes of the away side asymmetry for different trigger flavours was interpreted as a variation in the composition of parton subprocesses leading to pion or kaon triggers. Provided this is a correct assumption, this should also result in a different charge structure of the away jet. In Fig.5.28 the measured charge ratio $R^{+/-}$ in the away region is shown as a function of x_E for events with a trigger particle at $\Theta^{tri} \approx 45°$ and a transverse momentum above 4 GeV/c.

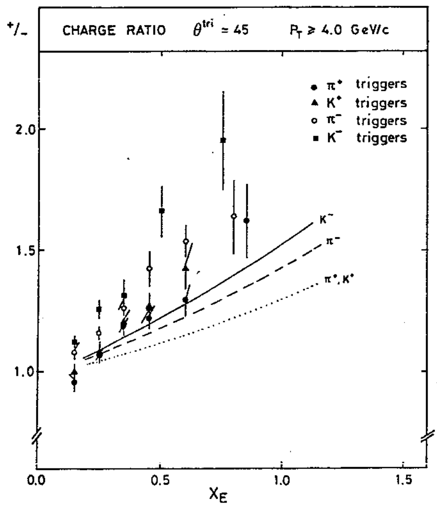

Fig.5.28: Charge ratio $R^{+/-}$ for different trigger particles produced at 45° with $p_T^{tri} \geq 4$ GeV/c. Lines are predictions from the LUND program (BEN85).

A clear dependence on the flavour of the trigger particle can be observed. The ratio is always increasing with x_E but is significantly larger in the case of K^- triggers than it is for π^+ triggers or K^+ triggers which are equal within the experimental errors. This reflects the same hierarchy as already observed for the away side asymmetry and it indicates that away jets associated with a K^- trigger have a higher valence quark contribution than away jets associated with a π^+ or K^+ trigger. The lines included are predictions from the LUND Monte-Carlo program using independent jet fragmentation. The predictions show clearly the same trend as the data but the absolute values are significantly predicted too low for all trigger flavours. The use of a different fragmentation mechanism, for instance the standard LUND string fragmentation, did not change the charge ratio significantly. All available fragmentation models fail to describe the inclusive distributions and the charge structure of the away jet. Again, the lack of gluon bremsstrahlung in the used models can explain qualitatively the difference between the experimental results and the predictions. Due to the higher ratio of gluon bremsstrahlung, gluon jets lose, on the average, more energy than quark jets. As a result, particles at large x_E are dominated by fragments of scattered valence quarks, leading to a large charge ratio. Another speculative possibility is the introduction of di-quark scattering into the simulation (for the model see: BRE85a). A detailed study on the effects of di-quark scattering was performed in ref. (LOH85) and it was shown that di-quark scattering cannot account for the differences between the measured charge ratios and the model predictions.

A comparison with the results from another ISR experiment is shown in Fig.5.29 where the charge ratios are shown for π^+ triggers at $\Theta^{tri} \approx 45^0$ and 90^0 (AKE84b).
The agreement is good between the two experiments and no obvious angular dependence between these two polar angles can be observed. To get an idea about the magnitude of the change of the charge ratio if the relative contribution of away side quarks is changed, the charge ratio for simulated events are included in Fig.5.29 for a relative quark to gluon contribution of 0% and 100%. The program used for the simulation was the LUND program with independent jet fragmentation. Because the absolute values of the predictions are always significantly lower than the experimental results, it is not possible to extract reliable numbers for the relative quark contribution from these ratios, but the trend is clearly visible to have a higher abundance of positive secondaries in quark jets than in gluon jets for which the charge ratio is constant around 1 as one would expect for a neutral parton.

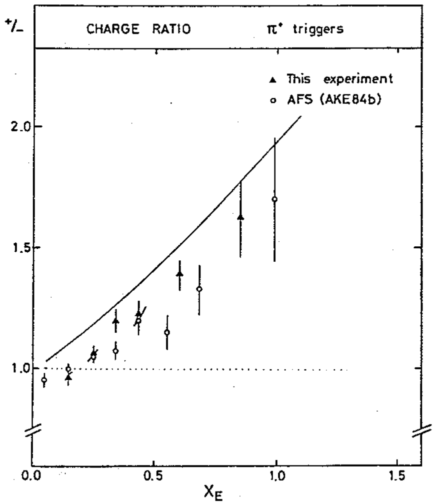

Fig.5.29: Charge ratios $R^{+/-}$ as a function of x_E for π^+ triggers at 45° (this experiment) and around 90° (AKE84b).
Lines are predictions from the LUND program for different quark contributions.

Charge ratio for different kinematical configurations

The measurement of the asymmetry indicated that a quark-gluon contribution exists as well as a strong quark-quark contribution for positive trigger particles. The away side gluons should be concentrated in the back-to-antiback region and the away side quarks should be found in the back-to-back hemisphere. This would yield a different charge structure of these two regions. Therefore in Fig.5.30 the charge ratio $R^{+/-}$ for π^+ triggers is plotted separately for the back-to-back and the back-to-antiback region. It can be seen that a much higher ratio for the back-to-back hemisphere than for the back-to-antiback region is found.

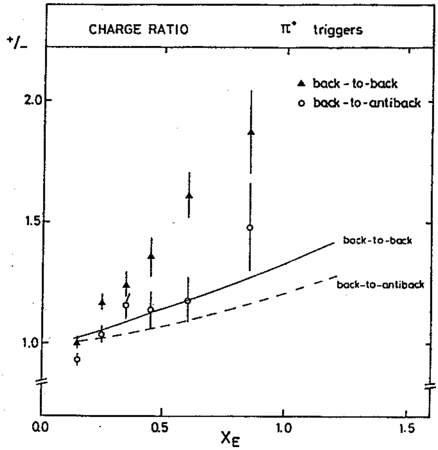

Fig.5.30: Charge ratios in the away jet as a function of x_E for π^+ triggers at 45°, separately for back-to-back and back-to-antiback. Lines are predictions from the LUND program with independent fragmentation.

This supports indeed the idea that away side quarks are mainly found in a back-to-back configuration to the trigger jet. The lines are predictions from the LUND program using independent jet fragmentation. They show the same bahaviour as the data although the absolute values are underestimated as one could already expect from the inspection of Fig.5.28. Exactly the same behaviour should be found for K^+ triggers if they are both produced by the same parton-parton scattering process. This is demonstrated in Fig.5.31 where the charge ratio is now plotted for K^+ triggers for the two configurations separately.

The comparison between Fig.5.30 and Fig.5.31 shows that the corresponding distributions are almost identical within the errors, giving further confidence in the hard scattering picture.

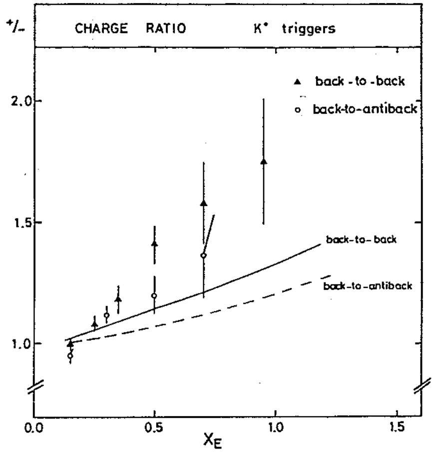

Fig.5.31: Charge ratio in the away jet as a function of x_E for K^+ triggers at 45°, separately for back-to-back and back-to-antiback.

A different result is expected if the trigger particle is the fragment of a scattered gluon with a dominant contribution of quark jets on the away side. The distributions for the back-to-back and the back-to-antiback regions are plotted in Fig.5.32 for events with a K^- trigger particle.
From Fig.5.28 it could be expected that the charge ratios are larger than for positive triggers due to a higher quark contribution on the away side. The comparison between the two regions shows that the values of the charge ratios are now reversed: The charge ratio is larger in the back-to-antiback region than in the back-to-back region. This can be interpreted as a large contribution of quark jets in the back-to-antiback region and this configuration is indeed favoured by the kinematics of a quark-gluon scattering process, where the gluon jet contains the trigger particle.

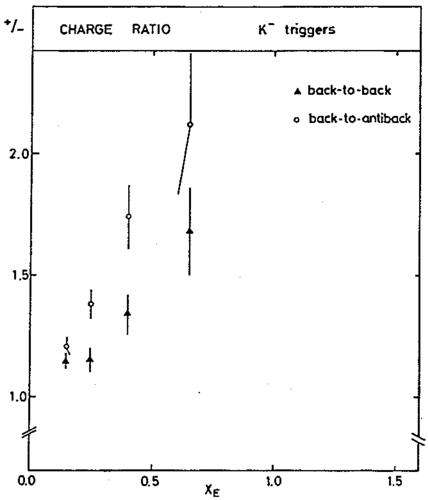

Fig.5.32: Charge ratio in the away jet as a function of x_E for K^- triggers at 45°, separately for back-to-back and back-to-antiback.

Charge ratio for different polar angles of the trigger particles

In a previous chapter it has been shown that the x_E-distributions for $\Theta^{tri}\approx 20°$ differ from those for $\Theta^{tri}\approx 45°$. It was speculated that this is due to a higher gluon contribution on the away side for the forward angles. To investigate this angular dependence of the contribution of the different subprocesses, the charge ratio $R^{+/-}$ for the away side secondaries is shown in Fig.5.33 for π^+ triggers at $\Theta^{tri}\approx 45°$ and 20°. The ratio $R^{+/-}$ is slightly lower for trigger particles at 20°.

This is supported in Fig.5.34 where the charge ratios are displayed separately for the back-to-back and the back-to-antiback regions.
In contrast to the ratios for π^+ triggers at 45° both ratios are almost identical.
A comparison with events with a trigger particle at 45° is performed in Fig.5.35 and Fig.5.36 where the ratios in the back-to-back and the back-to-antiback regions are compared to the corresponding ratios for positive triggers at $\Theta^{tri}\approx 45°$ with a transverse momentum between 2.0 GeV/c and 4.0 GeV/c.

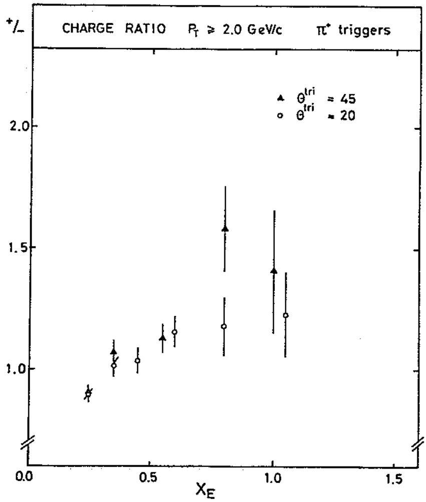

Fig.5.33: Charge ratios as a function of x_E for π^+ triggers at 45° and 20°.

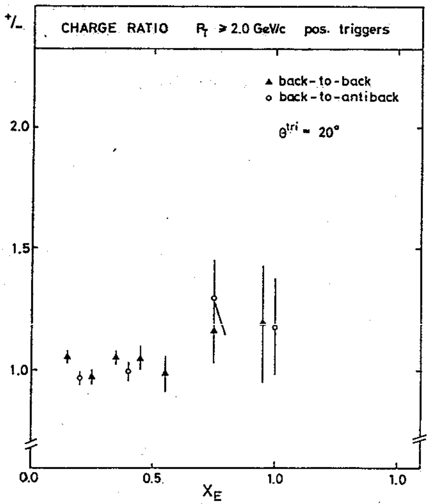

Fig.5.34: Charge ratios for positive triggers at 20° separately for the back-to-back and the back-to-antiback regions.

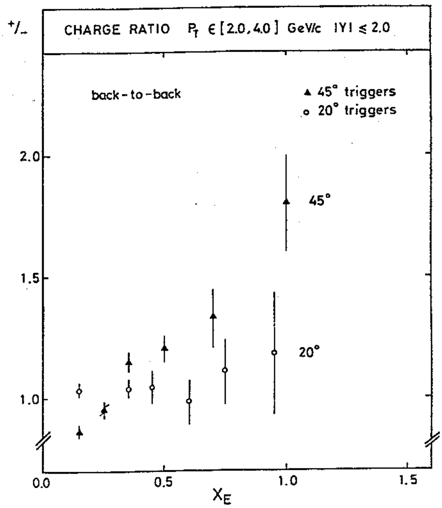

Fig.5.35: Charge ratios for positive triggers at 20° and 45° for the back-to-back regions.

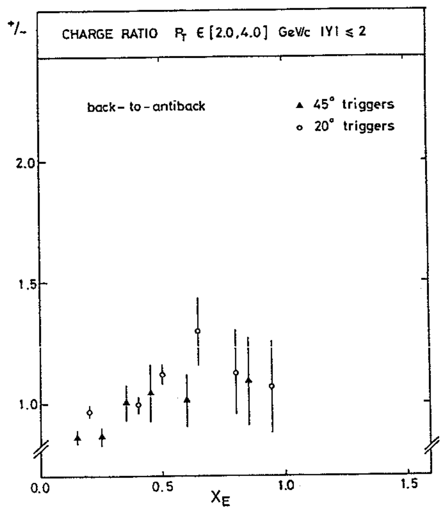

Fig.5.36: Charge ratios for positive triggers at 20° and 45° for the back-to-antiback regions.

While the ratios in the back-to-antiback region are identical within the experimental errors, the ratios in the back-to-back region are significantly larger for triggers at 45° indicating a stronger quark-quark scattering contribution. Such a angular dependence is also expected from QCD model calculations. The ratios in the back-to-antiback configuration show no distinct angular dependence and the ratios are close to unity indicating a strong gluon contribution for both values of the trigger polar angle investigated.

5.3.6 Comparison with measurements from other experiments

In this section an attempt will be made to relate the measured x_E-distributions to inclusive particle spectra measured for e^+e^- annihilations and with large transverse energy triggers in hadron-hadron collisions at the ISR and at the SppS collider.

To compare z-distributions, e.g. from e^+e^- annihilations, with the x_E-distributions, it is necessary to take into account the influence of the "trigger bias", since x_E is related to the trigger transverse momentum and not to the transverse momentum of the jets. It is not possible to determine the trigger bias for each individual event but the measured x_E-distributions can be globally corrected using the average value $\langle z^{tri}(p_T^{tri})\rangle$ as presented in section 4.6.3. This should be a reasonable approximation to the correct fragmentation variable x:

$$x = p/p_{jet};\ x_E \rightarrow x_E' = x_E \cdot \langle z^{tri}(p_T^{tri})\rangle$$

In Fig.5.37 the distribution $1/N \cdot dN/dx_E'$ for charged particles for π^+ triggers at $\Theta^{tri} \approx 45°$ is shown together with the distributions $1/N_{jets} \cdot dN/dz$ for charged particles measured for $p\bar{p}$ collisions at the $Sp\bar{p}S$ collider (ARN83b) and at the ISR with the AFS spectrometer (AKE84). The inclusive variable z has been chosen as:

$$z = p_L(\text{jet axis})/E(\text{jet}) \qquad 0 \lesssim z \lesssim 1$$

where p_L(jet axis) is the momentum of the charged particle projected on the jet axis and E(jet) is the total jet energy. All distributions are absolutely normalized.

Since the jets at the $Sp\bar{p}S$ collider are mainly gluon jets and the jets at the ISR are mainly quark jets at higher p_T^{tri}, this comparison should be treated only as a demonstration. Despite the very different c.m.s. energies of the experiments the agreement between the distributions is surprisingly good and encourages a comparison with z-distributions obtained in e^+e^- annihilations.

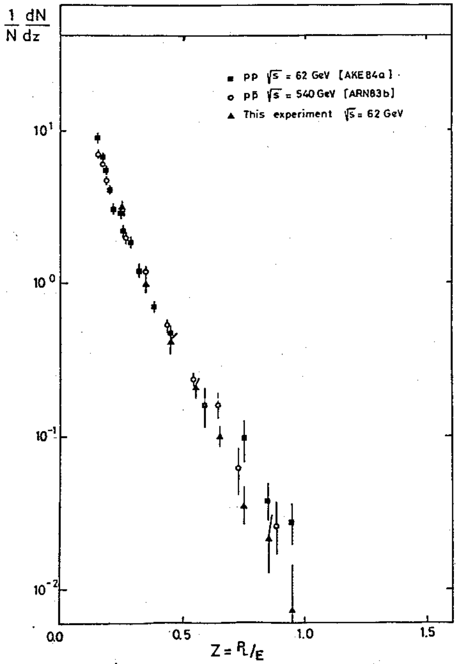

Fig.5.37: Inclusive x_E'-distribution for π^+ triggers at 45° compared with z-distributions from UA1 and AFS.

The inclusive z-distributions ($z = 2E/W$) measured with the TASSO (BRA82c) detector at c.m.s. energies of W = 22 GeV and W = 14 GeV are shown in Fig.5.38 together with our x_E'-distributions for π^+ triggers at 45°. These e^+e^- c.m.s. energies are a good approximation to the parton-parton c.m.s. energy in our hard proton-proton collisions. With an average $p_T^{tri} \approx 4.7$ GeV/c and $\langle z^{tri} \rangle \approx 0.75$ for trigger particles at 45° the c.m. energy of the parton interaction in the parton-parton rest system ranges from $\sqrt{s}$ = 14 to 25 GeV. The x_E'-distributions are normalized to the total cross section $\sigma_{e^+e^-} \rightarrow$ hadrons for this comparison using a value of 11/3 for R and taking into account that only one of the two transverse jets is used.

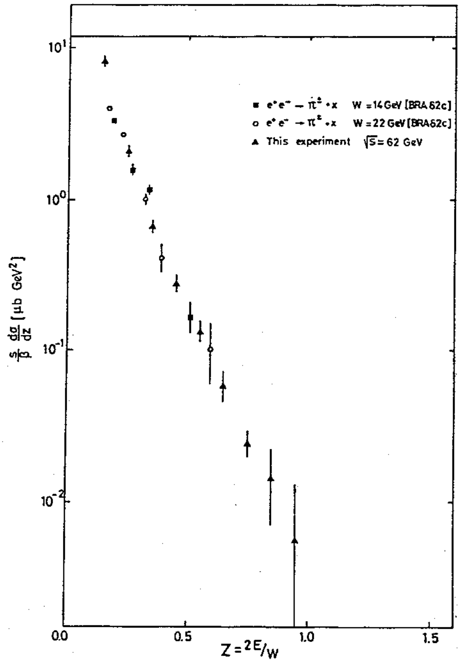

Fig.5.38: Inclusive x_E'-distributions normalized to the total cross section for hadron production in e^+e^- collisions together with the z-distribution measured at the TASSO detector at W = 22 GeV and 14 GeV (BRA82c).

Although the correction for the trigger bias is only an approximation to the "truth", the slope of the distribution as well as the absolute order of magnitude agrees astonishingly good.

It is not the intention of this section to quantitatively compare inclusive distributions from different types of experiments but rather to prove that the choice of the variable x_E is justified to study fragmentation properties of high-p_T jets. The small disadvantage of not knowing the total jet energy is overwhelmingly compensated by the additional information available which enables us to identify the scattered partons which allows the study of a rich field of quantum number correlations within and between the jets.

6. CONCLUSIONS

The production of high-p_T particles can be understood as the result of a hard elastic scattering process between the hadron constituents and their subsequent fragmentation into observable particles. The consequences of this hard scattering picture have been investigated in this analysis. The expected four-jet structure had been established earlier by experiments selecting events with a particle with large transverse momentum and more recently by experiments with large transverse energy triggers. With this experiment a clear four-jet structure was demonstrated for events with high-p_T particles produced at polar angles around Θ = 10°, 20°, and 45°. With the introduction of an interaction theory like QCD one would expect perturbative effects like scaling violations and gluon bremsstrahlung. Those effects have been observed in deep inelastic scattering and in e^+e^- annihilations and have increased the confidence in this picture. The gluons, mediating the strong interaction between the partons in the framework of QCD, now appear as hadron constituents and complicate the hard scattering picture since both, quarks and gluons, can participate in the scattering process. It is of great interest to study the properties of these jets and to compare it to the expectations. It was argued that the selection of events with a particle with large transverse momentum is a good tool for such studies. In section 4.6 it has been demonstrated that the identification of the high-p_T particle and the study of the charge structure of the trigger jet allows to draw conclusions about the scattered partons with a high level of confidence. So it was possible to associate scattered u - or d - quarks with high-p_T π^+ or π^- trigger particles. A possible coherent scattering of a bound di-quark system was deduced from the rate of high-p_T baryon production within the trigger jet. Those correlations have been studied intensively by our collaboration in the last years and a series of results was listed in 4.6 since they were essential for the argumentation in the following chapter.

To distinguish between the basic processes quark-quark, quark-gluon, and gluon-gluon scattering one has to identify simultaneously the second scattered parton which fragments into the away jet secondaries. The investigation of the spectator jets would then round off the analysis of high-p_T events to give a consistent picture. These later tasks to identify the away and spectator partons are more difficult than for the trigger jet since they do not contain a leading particle.

The study of away jet properties was the main aim of this work to contribute to the global analysis.

Two properties of the away jet have been used to approach this aim. While the position of the trigger jet is almost fixed in space by the trigger conditions the position of the away jet is determined by the kinematics of the interacting partons and therefore varies from event to event. Since quarks and gluons have a different structure function for the proton the interactions between two proton valence-quarks have different a kinematics than the interactions of a quark with a gluon. Two jets from partons with approximately equal longitudinal momenta result in a roughly colinear structure which was called the back-to-back configuration. The back-to-antiback configuration would be the result of a scattering process between two partons with substantially different longitudinal momenta. The main difference to those studies about the trigger jet is the necessity to study the trigger jet and the away jet simultaneously.

All studies were performed in terms of the inclusive variable x_E defined as the fraction of trigger transverse momentum balanced by an away side secondary particle. It has been shown to be a good approximation to the correct scaling variable which is not accessible for this type of experiment.

At the limit of large x_E the away jet shows a similar behaviour as the trigger jet since the selection of particles with large x_E is equivalent to the selection of a leading particle in the jet.

The asymmetry expected from different parton kinematics has been investigated using a variable R measuring the relative particle density in the back-to-back and the back-to-antiback regions as a function of x_E. The analysis of events with π^+ trigger particles produced around $\Theta = 20^\circ$ and 45° showed a different asymmetry for different transverse momenta of the trigger particle indicating an increasing relative contribution of quark-quark scattering when the transverse momentum of the trigger particle is increased. It has been proven that this is not a purely kinematical effect due to simple momentum conservation which should give the same effect for all different types of trigger particles, i.e. for all particle flavours. The data shows that the asymmetry indeed strongly depends on the flavour of the trigger particle. Events with π^+ trigger particles, most probably fragments from a scattered u-quark, show a much larger asymmetry than events with K^- trigger particles mostly coming from gluons. This is in good qualitative agreement with the expectations from the kinematics for quark-quark and quark-gluon scattering.

The next step of the analysis was to study the charge structure of the away jet which should on the average resemble the charge of the scattered parton.

The mean charge of the away jet should be zero if a gluon was scattered out and should reflect the quark contents of the parton in case of valence quark scattering.

The p_T-dependence of the asymmetry, which was interpreted as an increase of the relative importance of valence quark scattering, should be reflected by the p_T-dependence of the charge structure of the away jet if this interpretation was correct. The charge structure of the away jet was studied using the charge ratio of positive to negative secondaries in the away jet and the study was performed as a function of the variable x_E. A strong p_T-dependence was found for events with a π^+ trigger particle produced at polar angles around $\Theta = 45°$. The ratio of positive to negative secondaries in the away jet is a function rising in x_E and the absolute values are increasing as the trigger transverse momenta are increased. At this stage it was already possible to claim say that hard scattering with high-p_T π^+ production is most probably the result of quark-quark scattering when the away jet is in a back-to-back configuration to the trigger jet. The direct comparison of the charge ratios showed a much larger positive ratio in the back-to-back region than in the back-to-antiback region. This is in very good agreement with the expectations if the assumption of dominant quark-quark scattering was right. The same observations have been made for events with K^+ triggers which are also assumed to be produced from a scattered u-quark and should therefore show no differences for the away side structure compared to events with π^+ triggers.

The dependence on the flavour of the trigger particle of the away side charge ratio shows a similar hierarchy as the asymmetry and indicate that K^- triggers enrich quark jets on the away side and π^+, K^+, and, to a certain extent, π^- triggers enrich gluon jets recoiling against the trigger jet. The largest charge ratios are found for the back-to-antiback region for events with K^- trigger particles corresponding to a quark-gluon scattering process where the quark jet is found in the same hemisphere as the gluon jet containing the K^- trigger particle.

From QCD calculation one expects a polar angle dependence of the different scattering amplitudes. For the forward polar angles investigated ($\Theta^{tri} = 20°$) the Bjorken x of the scattered parton is very large and mainly quark jets will produce the trigger jet. On the away side a larger gluon component is expected which would result in a smaller charge ratio close to one. This has been found in the data. The charge ratios for trigger particles at $\Theta = 20°$ are smaller than those for triggers at $\Theta = 45°$ when compared for events with similar trigger transverse momenta. Although it is difficult to directly compare those different angles since the trigger bias is significantly different, the trend to a more neutral ratio for smaller polar angles is evident from the data.

The comparison of the result with model calculations was performed using the LUND Monte-Carlo program with independent fragmentation of the partons. This non-standard fragmentation scheme for the LUND program was chosen to identify secondaries which originated from the away parton only. Standard LUND string fragmentation was used for a comparison and did not change the results significantly.

Neither the slope nor the absolute values of the x_E-distributions can be correctly predicted by the model. The slope is significantly smaller than the observed one. The predictions could be improved by the introduction of initial and final state gluon bremsstrahlung into the model. This would result in a steeper distribution for the model predictions and they would approach the experimental results.

The charge ratios are predicted too low for all transverse momenta of the trigger particle and all types of the trigger particle although they show the same trends and dependencies as the experimental results. The introduction of gluon bremsstrahlung is probably necessary to improve the predictions for the charge ratios significantly.

The sum of all these results is a piece in the global analysis of events with high-p_T particles which was performed at the ISR in the last years. Together with the analysis of the trigger jet and the spectator jets and the study of correlations between those jets, it should be possible to disentangle the parton subprocesses leading to high-p_T events.

7. REFERENCES

ABR64 G.S. Abramss et al., Phys. Rev. Lett. 13 (1964) 670.
ABR82 H. Abramowicz et al., Z. Phys. C12 (1982) 289.
ABR83 H. Abramowicz et al., Z. Phys. C17 (1983) 283.
AKE82 T. Åkesson et al., Phys. Lett. 118B (1982) 185 and 193.
AKE83 T. Åkesson et al., Phys. Lett. 123B (1983) 133.
AKE84a T. Åkesson et al., CERN EP/84-56.
AKE84b T. Åkesson et al., Nucl. Phys. B246 (1984) 408.
ALB78 M.G. Albrow et al., Nucl. Phys. B145 (1978) 305.
M.G. Albrow et al., Nucl. Phys. B160 (1978) 1.
ALI80 A.Ali et al, Phys. Lett. 93B (1980) 155.
ALL83 P. Allen et al., Nucl. Phys. B214 (1983) 369.
ALO80 J.L. Alonso et al., Z. Phys. C6 (1980) 21.
ALP73 B. Alper et al., Phys. Lett. 44B (1973) 521.
ALP75 B. Alper et al., Nucl. Phys. B100 (1975) 237.
ALT77 G. Altarelli and G. Parisi, Nucl. Phys. B126 (1977) 298.
AND79a B. Andersen et al., Phys. Lett. 83B (1979) 379.
AND79b B. Andersen et al., Phys. Lett. 85B (1979) 417.
AND80a B. Andersen et al., Z. Phys. C3 (1980) 223.
AND80b B. Andersen et al., Z. Phys. C6 (1980) 235.
AND80c B. Andersen et al., Phys. Lett. 94B (1980) 211.
ANG78 A.L.S. Angelis et al., Phys. Lett. 79B (1978) 505.
ANG79 A.L.S. Angelis et al., Phys. Scr. 19 (1979) 116.
ANG81 A.L.S. Angelis et al., Phys. Lett. 98B (1981) 115.
ANG82 A.L.S. Angelis et al., Nucl. Phys. B209 (1982) 284.
ANG83 A.L.S. Angelis et al., Phys. Lett. 126B (1983) 132.
ARN83a G. Arnison et al., Phys. Lett. 123B (1983) 115.
ARN83b G. Arnison et al., Phys. Lett. 132B (1983) 223.
BAG83 P. Bagnaia et al., Z. Phys. C20 (1983) 117.
BAN73 M. Banner et al., Phys. Lett. 44B (1973) 537.
BAS79a A. Bassetto et al., Phys. Lett. 83B (1979) 207.
BAS79b A. Bassetto et al., Phys. Lett. 86B (1979) 366.
BAS80 A. Bassetto et al., Nucl. Phys. B163 (1981) 477.
BEL75 W. Bell et al., Nucl. Instr. and Meth. 124 (1975) 437.
BEL78 W. Bell et al., Nucl. Instr. and Meth. 156 (1978) 111.
BEN84 H.U. Bengtsson and G. Ingelman, LU-TP 84-3.

BEN85 H.U. Bengtsson and G. Ingelman, Comp. Phys. Comm. 34 (1985) 251.

BER70 S.M. Berman and M. Jacob, Phys. Rev. Lett. 25 (1970) 1683.

BER71 S.M. Berman,J.D. Bjorken and J.B. Kogut, Phys.Rev.D4 (1971) 3388.

BER83 F. Bergsma et al., Phys. Lett. 123B (1983) 269.

BER84 F. Bergsma et al., Phys. Lett. 141B (1984) 129.

BGR83 Ch. Berger et al., Nucl. Phys. B214 (1983) 189.

BJO69a J.D. Bjorken, Phys. Rev. 179 (1969) 1547.

BJO69b J.D. Bjorken et al., Phys. Rev. 185 (1969) 1975.

BOC81 R. Böck, E. Pagiola, J. Zoll, CERN program library, "HYDRA reference manual", (1981).

BOU74 R.Bouclier et al., Nucl. Instr. and Meth. 115 (1974) 235.

BOU75 R.Bouclier et al., Nucl. Instr. and Meth. 125 (1974) 19.

BRA81a R. Brandelik et al., Phys. Lett. 100B (1981) 357,

BRA82c R. Brandelik et al., Phys. Lett. 113B (1982) 98.

BRO82 B. Brown et al., Phys. Rev. Lett. 49 (1982) 711.

BRE84a A. Breakstone et al., Z. Phys. C21 (1984) 321.

BRE84b A. Breakstone et al., Z. Phys. C23 (1984) 1.

BRE84c A. Breakstone et al., Z. Phys. C23 (1984) 9.

BRE84d A. Breakstone et al., Phys. Lett. 135B (1984) 505.

BRE84e A. Breakstone et al., Phys. Lett. 135B (1984) 510.

BRE84f A. Breakstone et al., Phys. Lett. 147B (1984) 237.

BRE84g A. Breakstone et al., Z. Phys. C25 (1984) 21.

BRE85a A. Breakstone et al., Z. Phys. C28 (1985) 335.

BRO73 S.J. Brodsky and G.R. Farrar, Phys. Rev. Lett. 31 (1973) 1153.

BRO79 S.J. Brodsky, Phys. Scr. 19 (1979) 154.

BRY73 P. Bryant, "Beam crossing angles at the ISR", SFM Internal Note (1977).

BUC82 C.D. Buchanan, Proc. XVIIth Rencontre de Moriond (1982),

BUE73 F.W. Buesser et al., Phys. Lett. 46B (1973) 471.

BUE75 F.W. Buesser et al., Phys. Lett. 56B (1975) 482.

BUE76 F.W. Buesser et al., Nucl. Phys. B106 (1976) 1.

BUR77 A.J. Buras et al., Nucl. Phys. B131 (1977) 308.

BUR78 A.J. Buras et al., Nucl. Phys. B132 (1978) 249.

CAL69 C.G. Callan, and D.J. Gross, Phys. Rev. Lett. 22 (1969) 156.

CLA78 A.G. Clark et al., Phys. Lett. 74B (1978) 267.

CLA79 A.G. Clark et al., Nucl. Phys. B160 (1979) 397.

COM77 B.L. Combridge et al., Phys. Lett. 70B (1977) 234.

CRO75 J.W. Cronin et al., Phys. Rev. D11 (1975) 3105.

DAK74 J.T. Dakin et al., SLAC-PUB-1421 (1974) (unpublished).

DEG79 J.G.H. de Groot et al., Z. Phys. C1 (1979) 143.

DEL75 M. Della Negra et al., Phys. Lett. 59B (1975) 401 and 481.

DEL76 M. Della Negra et al., Nucl. Phys. B104 (1976) 365.

DEL77 M. Della Negra et al., Nucl. Phys. B127 (1977) 1.

DRI76 D. Drijard, "Spline Track Fit", SFM internal note (1976).

DRI79 D. Drijard et al., Nucl. Phys. B156 (1979) 309.

DRI80 D. Drijard et al., Nucl. Phys. B166 (1980) 223.

DRI82a D. Drijard et al., Nucl. Phys. B208 (1982) 1.

DRI82b D. Drijard, SFM-Internal Note, (1982).

DRI83 D. Drijard et al., Phys. Lett. 121B (1983) 433,

ELL74 S.D. Ellis and M.B. Kislinger, Phys. Rev. D9 (1974) 2027.

ELL76 S.D. Ellis, M. Jacob, P. Landshoff, Nucl. Phys. B108 (1976) 93.

FEY69 R.P. Feynman, Phys. Rev. Lett. 23(1969) 1415.

FEY77 R.P. Feynman, R.D. Field, G.C. Fox,, Nucl. Phys. B128 (1977) 1.

FEY78 R.P. Feynman, R.D. Field, G.C.Fox, Phys. Rev. D18 (1978) 3320.

FIE77 R.D. Field and R.P. Feynman, Phys. Rev. D15 (1977) 2590.

FIE83 R.D. Field and S. Wolfram, Nucl. Phys. B213 (1983) 65.

FIS75 H.G. Fischer, CERN EF Internal Report (1975).

FIS81 H.G. Fischer, Proc. of the EPS Conference, Lisbon 1981, 897.

FOX80 G.C. Fox and S. Wolfram, Nucl. Phys. B168 (1980) 285.

FRE81 H. Frehse, "On-line filtering at the ISR" CERN 81-07 (1981) 301.

FRE82a S. Fredriksson et al., Z. Phys. C14 (1982) 35.

FRE82b S. Fredriksson et al., Z. Phys. C19 (1982) 53.

FRI73 H. Fritzsch, M. Gell-Mann, and H. Leutwyler, Phys. Lett. 47B (1973) 365.

GEL64 M. Gell-Mann, Phys. Lett 8 (1964) 214.

GES86 L. Gesswein, Diploma Thesis, Heidelberg University (1986).

GLU78 M. Glueck et al., Nucl. Phys. B145 (1978) 24.

GLU81 M. Glueck and E. Reya, Phys. Lett. 98B (1981) 444.

HAN76 P. Hanke, Ph. D. Thesis, Karlsruhe (1976).

HAN80 P. Hanke, "TOF calibration system", SFM Int. Note, (1980).

HEI82 M. Heiden, Ph. D. Thesis, Heidelberg University (1982).

HER82 W. Herr, "Cherenkov efficiency", SFM-Int. Note, (1982).

HOM76 D.C. Hom et al., Phys. Rev. Lett. 36 (1976) 1239.
D.C. Hom et al., Phys. Rev. Lett. 37 (1976) 1374.

HOY79 P.Hoyer at el., Nucl. Phys. B161 (1979) 349.

ING84 G. Ingelman, Z. Phys. C26 (1984) 483.

JAC76 M. Jacob and P. Landshoff, Nucl. Phys. B113 (1976) 395.

KLE83 H. J. Klein, J. Zoll, CERN program library, "Patchy Reference Manual",October 1983.

KOG74 J. Kogut and L. Susskind, Phys. Rev. D9 (1974) 697.

KOR76 V. Korbel, "SFM Cherenkov counters", SFM-Int. Note (1976).

KUN76 P.F. Kunz et al, Nucl. Instr. and Meth. 135 (1976) 435.

LAR84 T.I. Larsson, Phys. Rev. D29 (1984) 1013.

LOH82 T. Lohse, Diploma Thesis, Dortmund University (1982).

LOH85 T. Lohse, Ph. D. Thesis, Dortmund University (1985).

MAT73 V.A. Matveev et al., Let. Nuovo Cim. 7 (1973) 719.

MES78 R. Messerli, CERN Hydra Application Library, "SIMU, a general purpose simulation program".

MET74 M. Metcalf, DM Developement Note AP-10 (1974).

MEY80 W.T. Meyer, "SFM Cherenkov counters", SFM-Int. Note (1980).

MUS78 J. Musset and J.P. Vialle, Phys. rep. 39C (1978) 1.

NAK83 T. Nakada, Ph. D. Thesis, Heidelberg University, (1983).

NOR78 A. Norton, "Local Track Finding", SFM-Int. Note (1978).

PAN82 M. Panter, Ph. D. Thesis, Dortmund University, (1982).

POL73 H.D. Politzer, Phys. Rev. Lett. 30 (1973) 1346.

RAU82 K. Rauschnabel, Ph. D. Thesis, Dortmund University, (1982).

REN85 B. Rensch, Diploma Thesis, Heidelberg University, (1985).

REY79 E. Reya, DESY 79/88 (1979).

SAJ80 G. Sajot, These de doctorat, Paris University, (1980).

SIV76 D.I. Sivers et al., Phys. Rep. 23C (1976) 1.

SJO82 T Sjostrand , LU TP 82-3 (1982).

SPA82 J.F. Spahn, Ph. D. Thesis, UCLA, (1982).

STE75 S. Stein et al., Phys. Rev. D 12 (1975) 1884.

SZC82 M. Szczekowski, SFM Internal Note (1982).

VDM68 S. Van der Meer, CERN ISR-PO/68-31 (1968).

WEB83 B.R. Webber, CERN preprint TH-3569 (1983).

WIN72 H. Wind, Proc. CERN Computing and Data Processing School, CERN 72-21 (1972).

WIN73 H. Wind, CERN/NP/DHG 73-5 (1973).

WIN74 H. Wind, Nucl. Instr. and Meth. 115 (1974).

WUS84 S.L. Wu, DESY 84-028 (1984).

ZWE64 G. Zweig, CERN TH-401,CERN TH-412, (1964).

8. ACKNOWLEDGEMENTS

This work was performed within the Ames-Bologna-CERN-Dortmund- Heidelberg-Warsaw collaboration.

I would like to thank all members of the collaboration for their contributions and collegial assistance during the period of this work. Without them this work would not have been possible.

I am particularly grateful to my advisor Prof Dr E.E. Kluge at Heidelberg for his guidance, a continous support and his lasting interest in my work.

I am also very much indebted to Dr A. Putzer whose enormous experience was a great help for my everyday work. His engagement was also essential for a successful accomplishment of processing a large amount of data at Heidelberg while I was at CERN. I also like to thank him for his critical reading of the manuscript.

I would like to express my gratefulness to Dr D. Drijard and Dr H.G. Fischer for their patient guidance and innumerable discussions during my stay at CERN.

For the permanent help to overcome daily problems and their friendly advices, suggestions and - sometimes necessary - stimulations I would like to thank Dr W. Geist and Dr P. Hanke. Special thanks to Dr M. Heiden for his permanent help when I was stuck in the debris of SFM-software or fighting against fatal polycephalous monsters as well as to Dr T. Lohse for his desparate attempts to overcome my ignorance about detailed theoretical problems and for many fruitful and nutritious discussions seven days a week.

It is impossible to mention everybody explicitly who has contributed to the successful execution of this work and the good working conditions. My sincere to all those people.

At this place I would like to thank Mrs E. Konrad and Mrs I. Spinnler for their technical assistance in processing the vast amount of data and Mrs E. Konrad also for her accurate preparation of figures.

It is a pleasure and my special desire to thank the staff of the computer centre of the Institut für Hochenergiephysik for providing a powerful computing facility and a friendly service over a period of several years.

Financial support from the Bundesministerium für Forschung und Technologie of the Bundesrepublik Deutschland and an occasional gratuity from CERN made it possible to survive with a reasonable living standard during the extended period of time I have spent at CERN in Geneva.

Last, but not least I would like to thank all the people who made a big effort to keep me in a good physical and psychical constitution over all the years. Although I know that any selection is somewhat arbitrary I would like to mention my parents, my girlfriend Nanette, and the fellows from our gang.

Thanks chaps.